von Neumann Stability Analysis of Globally Divergence-Free RKDG Schemes for the Induction Equation using Multidimensional Riemann Solvers

By

Dinshaw S. Balsara[1] **and Roger Käppeli**[2]

[1]Physics Department, University of Notre Dame, USA (dbalsara@nd.edu)

[2]Seminar for Applied Mathematics (SAM), Department of Mathematics, ETH Zürich,CH-8092
Zürich, Switzerland (roger.kaeppeli@sam.math.ethz.ch)

Abstract

In this paper we focus on the numerical solution of the induction equation using Runge-Kutta Discontinuous Galerkin (RKDG) -like schemes that are globally divergence-free. The induction equation plays a role in numerical MHD and other systems like it. It ensures that the magnetic field evolves in a divergence-free fashion; and that same property is shared by the numerical schemes presented here. The algorithms presented here are based on a novel DG-like method as it applies to the magnetic field components in the faces of a mesh. (I.e., this is not a conventional DG algorithm for conservation laws.) The other two novel building blocks of the method include divergence-free reconstruction of the magnetic field and multidimensional Riemann solvers; both of which have been developed in recent years by the first author.

Since the method is linear, a von Neumann stability analysis is carried out in two-dimensions to understand its stability properties. The von Neumann stability analysis that we develop in this paper relies on transcribing from a modal to a nodal DG formulation in order to develop discrete evolutionary equations for the nodal values. These are then coupled to a suitable Runge-Kutta timestepping strategy so that one can analyze the stability of the entire scheme which is suitably high order in space and time.

We show that our scheme permits CFL numbers that are comparable to those of traditional RKDG schemes. We also analyze the wave propagation characteristics of the method and show that with increasing order of accuracy the wave propagation becomes more isotropic and free of dissipation for a larger range of long wavelength modes. This makes a strong case for investing in higher order methods. We also use the von Neumann stability analysis to show that the divergence-free reconstruction and multidimensional Riemann solvers are essential algorithmic ingredients of a globally divergence-free RKDG-like scheme.

Numerical accuracy analyses of the RKDG-like schemes are presented and compared with the accuracy of PNPM schemes. It is found that PNPM retrieve much of the accuracy of the RKDG-like schemes while permitting a larger CFL number.

I) Introduction

Several important problems in science and engineering rely on the MHD system of equations. This class of PDEs can indeed be written in a conservation law form. As a result, methods that have been developed for the treatment of hyperbolic conservation laws are indeed applicable to them. For MHD, the electric field can be written as $\mathbf{E} = -\mathbf{v} \times \mathbf{B}$ and it governs the divergence-free evolution of the magnetic field. In two dimensions, $\mathbf{B} = B_x \hat{x} + B_y \hat{y}$ is the magnetic field and $\mathbf{v} = \mathrm{v}_x \hat{x} + \mathrm{v}_y \hat{y}$ is the velocity. The update of the magnetic field takes place according to the induction equation:

$$\frac{\partial \mathbf{B}}{\partial t} - \nabla \times \left(\mathbf{v} \times \mathbf{B} \right) = 0 \tag{1.1}$$

In this paper we develop a von Neumann stability analysis for RKDG schemes that are used to solve eqn. (1.1). Because such an analysis would be very difficult in three dimensions, most of this paper describes a two-dimensional situation. Because magnetic monopoles have not been detected in nature, the magnetic field starts off divergence-free; i.e., $\nabla \cdot \mathbf{B} = 0$. The above induction equation then ensures that the magnetic field remains divergence-free for all time. It is highly desirable to satisfy this divergence-free constraint in a numerical code because it provides maximum consistency with the physics ([51], [23], [24]). It is easy to see that the divergence of a vector field is a topological constraint that is an integral part of the PDE system. Numerical methods that preserve, in a discrete sense, the symmetries and constraints that are true for the continuum PDE are referred to as mimetic schemes. A mimetic scheme for the induction equation should keep the divergence of the vector field zero on the computational mesh, because the PDE itself has this property. Mimetic schemes for the induction equation, therefore, follow a Yee-style collocation of variables with the magnetic field components collocated at face centers and the electric field components at edge centers of a mesh. For that reason, please note that we are not presenting a conventional Discontinuous Galerkin (DG) scheme for a conservation law that is defined on the elements of the mesh. Instead, we are describing a DG-like method for the induction equation that applies to magnetic field components that are defined on the *faces of the elements* of the mesh. (For the sake of nomenclatural clarity in the rest of the paper, we will distinguish between the magnetic field, which is a two or three component vector, and the component of the magnetic field, which is a scalar that is collocated at the faces of the mesh.)

Higher order Godunov methods have been developed for constraining the evolution of the magnetic field ([1], [2], [8], [9], [11], [12], [36], [36], [44], [4], [42], [37], [40], [70], [47], [26]). While early methods were based on one dimensional Riemann solver technology, it had been well-recognized that multidimensional Riemann solvers were needed for obtaining the electric field. Such multidimensional Riemann solvers have now been developed (Balsara [13], [14], [17], [19], Balsara, Dumbser & Abgrall [15] and Balsara & Dumbser [17], Vides *et al*. [48], Balsara *et al*. [21], [22]), opening the door to a more methodical analysis of eqn. (1.1) ([5], [6], [7], [20], [49]). MHD schemes that are positivity preserving have also been developed ([3], [18], [25]).

Discontinuous Galerkin (DG) schemes have seen much further development in the last two decades ([43], [27], [29], [28], [30], [10]). Coupled with strong stability preserving Runge-Kutta semi-discrete time-stepping schemes ([90], [91], [45], [46], [38], [39]) they take the acronym of RKDG schemes. Because of their simple structure, desirable stability properties, and the potentially high accuracy that they offer, RKDG schemes for fluid dynamics type problems have enjoyed considerable recent popularity. It is desirable to extend these ideas to divergence-free MHD and its analogous systems.

Thus the *first goal* of this paper is to design RKDG-like schemes for the induction equation that are based on the two building blocks – globally divergence free reconstruction and multidimensional Riemann solvers. DG schemes that are locally divergence-free within each element have been attempted by Cockburn *et al*. [32] and Li and Shu [42]. Such locally divergence-free schemes are divergence-free within each element, but they produce a jump in the normal component of the magnetic field at element boundaries. Globally divergence-free central DG schemes that operate on a pair of staggered meshes have been presented by Li *et al*. [40]. The present DG-like formulation differs from those early attempts in two respects. First, it is globally divergence-free at all points of mesh; this includes the interior of an element as well as its boundary. Second, it obtains the electric field at the edges through a direct application of a multidimensional Riemann solver. The *second goal* of this paper is to analyze the stability of the RKDG-like schemes for the induction equation using von Neumann stability analysis. In doing that, we follow the path set down by Zhang and Shu [52] and Liu et al. [41] who analyzed the stability of conventional RKDG schemes for scalar advection in one dimension. Because such analyses are intrinsically very difficult, we restrict attention to the two dimensional case. In two dimensions, the induction equation has a structure that is quite different from an advection equation. Yang and Li [50] have also analyzed the induction equation. However, their method is not based on the multidimensional Riemann solver approach used here. Instead, their work relies on an overlapping mesh approach. Furthermore, their analysis is restricted to first order schemes.

As the order of accuracy of an RKDG scheme is increased, the permissible CFL decreases. PNPM schemes (Dumbser *et al*. [35]) are one way of overcoming this problem. (PNPM schemes evolve an N^{th} order spatial polynomial, while spatially reconstructing higher order terms up to M^{th} order.) The *third goal* (which is a much smaller goal) of this paper is to show that PNPM schemes for the induction equation retrieve much of the accuracy of the RKDG-like schemes while permitting a larger CFL number.

The plan of the paper is as follows. Section II presents the DG-like formulation for the induction equation. Section III briefly describes the divergence-free reconstruction in a fashion that is suited for later use in the von Neumann stability analysis. Section IV develops multidimensional Riemann solvers for the induction equation and explicitly discusses their dissipation characteristics. Such a discussion enables us to show that the multidimensional Riemann solvers are always stabilizing. Section V shows how the von Neumann stability analysis is carried out by using first order (i.e., P=0) and second order (i.e., P=1) DG schemes with various orders of Runge-Kutta timestepping as a detailed example. Once the second order case is understood, the extension of the von Neumann stability analysis to even higher orders is quite easily done with the help of a computer algebra system. Section VI presents the results of the von Neumann stability analysis for the RKDG-like scheme for the induction equation. Section VII provides results from accuracy analysis of the resulting linear RKDG-like schemes and compares them to PNPM schemes for the induction equation. Section VIII presents some conclusions.

II) DG Formulation for the Induction Equation

It is very important to begin by pointing out that the method presented here is not a conventional DG scheme for conservation laws. However, it shares many philosophical features with a conventional DG scheme, which is why we call it a DG-like scheme. A compare and contrast between a conventional DG scheme for conservation laws and the DG-like scheme for the induction equation (that is presented in this paper) would be most useful. The compare and contrast is presented in pointwise fashion below:

1) DG schemes for conservation laws are based on projecting the solution within an element onto a set of trial functions that are defined within the same element. The coefficients of those trial functions form the primal variables of the DG scheme. The DG-like scheme for the induction equation that is presented here uses the components of the magnetic field, and their higher moments, that live within the *faces* of each element as the primal variables. The corresponding trial functions are also defined within the faces of each element.

2) In a conventional DG scheme for conservation laws a vector identity associated with the divergence is applied to the product of a test function and the flux. By contrast, in the present DG-like scheme for the induction equation we apply a vector identity associated with the curl to the product of the test function and the facial magnetic field component.

3) Consequently, in a conventional DG scheme for conservation laws, the update equations for the zone-centered flow variables and their higher moments depends on the fluxes at the zone boundaries as well as a volumetric integration term. In the present DG-like scheme for the induction equation, the update equations for the face-centered magnetic field components, as well as their higher order moments, depends on the electric fields at the vertices of the mesh and a further facial area-integrated term.

4) For a conventional DG scheme for conservation laws, the fluxes at the zone boundaries are obtained by using a weak form solution of the one-dimensional Riemann problems at the zone boundaries. In the present DG-like scheme for the induction equation, the electric fields at the vertices of the mesh are obtained by using a weak form solution of the multidimensional Riemann problems at the vertices of the mesh.

We see that there are very close analogies between a conventional DG scheme for a conservation law and the DG-like schemes that we have developed for the induction equation. For that reason, we adopt a short form and refer to the DG-like schemes as DG schemes in the ensuing discussion.

Recall that DG schemes for conservation laws derive from the well-known vector identity

$$\nabla \cdot \left(\phi \, \mathbf{F} \right) = \phi \, \nabla \cdot \mathbf{F} + \mathbf{F} \cdot \nabla \phi$$

where $\mathbf{F}$ takes on the role of a flux and ϕ is a test function. Use of Gauss' theorem then yields a weak form update for the PDE, where the flux terms at the boundary of a zone are replaced with fluxes that are obtained from a Riemann solver. Clearly, the curl operator in eqn. (1.1) suggests the use of Stokes' theorem. This time, since each magnetic field component resides in a face of the mesh, we wish to use Stokes theorem within a face. To that end, we assert the well-known vector identity

$$\nabla \times \left(\phi \, \mathbf{E} \right) = \left(\nabla \phi \right) \times \mathbf{E} + \phi \, \nabla \times \mathbf{E} \tag{2.1}$$

within each face of the mesh. In this paper, and for the sake of simplicity, we use a two-dimensional Cartesian mesh with zones of size Δx and Δy in the x- and y-directions. Let $\hat{\mathbf{n}}$ be a unit normal to a face A_n . The governing equation is taken to be

$$\frac{\partial \mathbf{B}}{\partial t} + \nabla \times \mathbf{E} = 0 \tag{2.2}$$

In order to obtain the most general interpretation of eqn. (2.2), we think of applying this equation to a two-dimensional face of a three-dimensional mesh; please see Fig. 1 from Balsara [6]. We wish to project the governing eqn. (2.2) into a space of test functions. However, we need to devise a projection strategy that is applied to the faces of the mesh, this is done as follows. Our test functions are chosen to be identical to our trial functions. First we multiply the governing equation by the test function ϕ. Next, we restrict our attention to the face A_n by taking a dot product with the unit normal $\hat{\mathbf{n}}$ to that face. We then integrate over that face to get

$$\frac{\partial}{\partial t} \left(\int_{A_n} \left(\hat{\mathbf{n}} \cdot \mathbf{B} \right) \phi \, dA_n \right) + \int_{\partial A_n} \left(\phi \, \mathbf{E} \right) \cdot d\vec{\ell} - \int_{A_n} \hat{\mathbf{n}} \cdot \left[\left(\nabla \phi \right) \times \mathbf{E} \right] dA_n = 0 \tag{2.3}$$

The boundary of the face under consideration is denoted by ∂A_n.The infinitesimal vector $d\vec{\ell}$ in the middle term of eqn. (2.3) runs along ∂A_n and denotes the length of the element. The existence of a unit normal, $\hat{\mathbf{n}}$, lends a right-handed directionality to $d\vec{\ell}$. Eqn. (2.3) gives us the desired Galerkin projection strategy; but please realize that it applied to a curl-type equation in the faces of the mesh. Notice that the second term in eqn. (2.3) is interpreted in a weak form using a multidimensional Riemann solver and is analogous to the flux term in a traditional DG method for conservation laws. The third term in eqn. (2.3) is analogous to the volume term in a traditional DG method for conservation laws.

As with traditional DG methods, observe that when the test function is taken to be $\phi = 1$ we retrieve the traditional Yee-type update equation for the mean magnetic field within face A_n. The third term in eqn. (2.3) then becomes zero and we see that the mean magnetic field within a face is updated by the electric field that resides in the edges of that face. This electric field is obtained by using multidimensional Riemann solvers. For a three-dimensional problem, quadrature points can be chosen along each edge so that the middle term is evaluated with suitable accuracy by invoking multidimensional Riemann problems at each of those quadrature points. In two dimensions, the edge integral reduces to a single evaluation of the electric field at the vertices of the mesh for each sub-step in the Runge-Kutta method. When the test function is not unity, the third term in eqn. (2.3) also begins to contribute. The electric field that is to be used in the third integral of eqn. (2.3) can be obtained via one-dimensional Riemann problems that use the magnetic field on either side as inputs. (While the normal component of the magnetic field will not have a jump; the transverse component(s) will have a jump. This ensures that the Riemann solver can introduce dissipation as needed.) Notice too that having a perfect Yee-type update for the mean magnetic field is sufficient to ensure that the magnetic field remains divergence-free for all time.

It is easiest to appreciate eqn. (2.3) via some simple examples. In order to provide a point of reference to the reader, we catalogue the explicit update equations for the magnetic field components on a two-dimensional mesh. Let us say that a two-dimensional zone has an extent $\left[-\Delta x/2, \Delta x/2\right] \times \left[-\Delta y/2, \Delta y/2\right]$. Within the right face of this zone, let the x-component of the magnetic field have variation given by (i.e., we are explicitly providing the formulation of RKDG or PNPM schemes that are up to third order accurate):-

$$B^x\left(y,t\right)=B_0^x\left(t\right)+B_y^x\left(t\right)\left(\frac{y}{\Delta y}\right)+B_{yy}^x\left(t\right)\left(\left(\frac{y}{\Delta y}\right)^2-\frac{1}{12}\right) \tag{2.4}$$

In the above equation, the modes of the x-component of the magnetic field are endowed with time variation, just as in the traditional DG formulation. Also please note that the x-component is denoted with a superscript "*x*" because the subscripts are used to denote the modes. This is a very convenient notational simplification that is maintained throughout this paper. Using test functions that are identical to the trial (or basis) functions in eqns. (2.3) and (2.4), we obtain the update equations

$$\frac{dB_0^x\left(t\right)}{dt}+\frac{1}{\Delta y}\left(E^z\left(y=\Delta y/2\right)-E^z\left(y=-\Delta y/2\right)\right)=0 \tag{2.5a}$$

$$\frac{1}{12}\frac{dB_y^x\left(t\right)}{dt}+\frac{1}{2\Delta y}\left(E^z\left(y=\Delta y/2\right)+E^z\left(y=-\Delta y/2\right)\right)-\frac{1}{\Delta y}\left\langle E^z\left(y\right)\right\rangle=0 \tag{2.5b}$$

$$\frac{1}{180}\frac{dB_{yy}^x\left(t\right)}{dt}+\frac{1}{6\Delta y}\left(E^z\left(y=\Delta y/2\right)-E^z\left(y=-\Delta y/2\right)\right)-\frac{2}{\Delta y}\left\langle\left(\frac{y}{\Delta y}\right)E^z\left(y\right)\right\rangle=0 \tag{2.5c}$$

Eqn. (2.3) is crucially important for deriving the above equations. Here $E^z\left(y=\Delta y/2\right)$ and $E^z\left(y=-\Delta y/2\right)$ are electric field components that are obtained at the endpoints of the right face. They are obtained by the application of a multidimensional Riemann solver. Several concordances with traditional DG are readily visible from eqn. (2.5). For example, we see that the factors $1/12$, $1/180$ and $1/2800$ are analogous to a mass matrix. Because we have a Cartesian mesh with a mutually orthogonal set of trial/basis functions, our mass matrix is diagonal. Also notice that the terms within angled brackets, i.e. terms with $\langle\ \rangle$, represent line integrals within a face; these terms with an angled bracket are to be obtained with a suitably high order quadrature along each face of the mesh. In this work, we use the well-known one-dimension Gauss-Legendre quadrature to carry out the facial integrals; though see Stroud [52] for the two-dimensional integrals that are needed in three-dimensional formulations. One dimensional Riemann problems in the right face being considered will furnish the $E^{z}\left(y\right)$ component of the electric field that is to be used in the angled brackets. These one-dimensional Riemann problems are solved at each of the quadrature points in the face. Recall, that when the induction equation is coupled to the rest of the MHD system, the Riemann solvers will anyway have to be invoked in the faces just for updating the conserved variables. Consequently, a full-fledged RKDG or PNPM scheme will suffer from no loss in efficiency due to the invocation of the one-dimensional Riemann solvers in the faces of the mesh.

For the sake of completeness, let us also quickly write the y-component of the magnetic field in the top face of the zone being considered as

$$B^{y}\left(x,t\right)=B_{0}^{y}\left(t\right)+B_{x}^{y}\left(t\right)\left(\frac{x}{\Delta x}\right)+B_{xx}^{y}\left(t\right)\left(\left(\frac{x}{\Delta x}\right)^{2}-\frac{1}{12}\right) \tag{2.6}$$

As in eqn. (2.4), the modes in eqn. (2.6) have been endowed with time variation. Again using several test functions in eqn. (2.3) gives the update equations for the modes in eqn. (2.6). We get

$$\frac{dB_{0}^{y}\left(t\right)}{dt}-\frac{1}{\Delta x}\left(E^{z}\left(x=\Delta x/2\right)-E^{z}\left(x=-\Delta x/2\right)\right)=0 \tag{2.7a}$$

$$\frac{1}{12}\frac{dB_{x}^{y}\left(t\right)}{dt}-\frac{1}{2\Delta x}\left(E^{z}\left(x=\Delta x/2\right)+E^{z}\left(x=-\Delta x/2\right)\right)+\frac{1}{\Delta x}\left\langle E^{z}\left(x\right)\right\rangle=0 \tag{2.7b}$$

$$\frac{1}{180}\frac{dB_{xx}^{y}\left(t\right)}{dt}-\frac{1}{6\Delta x}\left(E^{z}\left(x=\Delta x/2\right)-E^{z}\left(x=-\Delta x/2\right)\right)+\frac{2}{\Delta x}\left\langle\left(\frac{x}{\Delta x}\right)E^{z}\left(x\right)\right\rangle=0 \tag{2.7c}$$

Eqns. (2.5) and (2.7) show us that the temporal update has been turned into a system of ODEs in each of the faces of the mesh. Consequently, it is appropriate to use strong stability-preserving Runge-Kutta timestepping schemes for the temporal evolution of the PDE. Eqns. (2.5a) and (2.7a) taken together also ensure that the mean magnetic field components within the faces of the mesh preserve the divergence-free property at a discrete level. This too is very analogous to the traditional RKDG schemes for conservation laws where the conservation is ensured by the lowest modes in the DG expansion.

III) Divergence-Free Reconstruction

This topic has already been described quite extensively in the literature by Balsara [5], [6], [7], Xu *et al.* [49] and Balsara and Dumbser [20]. Therefore, we only present sufficient information here for the second order case in two-dimensions. Some mathematical details of the second order accurate case have been catalogued in Appendix A. The third order accurate case is relegated to Appendix B. We describe the second order case here so that we may set the stage for the von Neumann stability analysis that follows in Section V. For a more thorough discussion, the reader is invited to look up the previously-cited references and the Appendices of this paper.

Fig. 1 shows how the divergence-free reconstruction is carried out in the shaded zone. The profiles of the facial magnetic field components are also shown. Fig. 1a shows piecewise constant magnetic field components in the faces; i.e., the first order case. Fig. 1b shows piecewise linear magnetic field components in the faces; i.e., the second order accurate case. The task of the divergence-free reconstruction is to reconstruct the magnetic field in a pointwise divergence-free fashion in the interior of the shaded zone. The reconstruction should be such that the magnetic field in the shaded region matches the magnetic field components in the bounding faces of this zone exactly.

We assume that Fig. 1 pertains to a reference square with extent $\left[-1/2,1/2\right]\times\left[-1/2,1/2\right]$. Let the mean magnetic field components in the right and left faces of Fig. 1 be denoted by $B_0^{x\pm}$ respectively. Similarly, let the mean magnetic field components in the top and bottom faces of Fig. 1 be denoted by $B_0^{y\pm}$ respectively. (Any rectangular element can be remapped to a reference square by suitable linear rescaling of the coordinates and the magnetic field components.) The field components are not independent since they are related by a discrete divergence-free condition. On the reference element, the discrete divergence-free condition is given by

$$\left(B_0^{x+}-B_0^{x-}\right)+\left(B_0^{y+}-B_0^{y-}\right)=0 \tag{3.1}$$

As a result, we see that the constant profiles in the faces of a zone in Fig. 1a only carry three independent pieces of information. Fig. 1a, which pertains to first order of accuracy, is only for informational purposes. The schemes of interest have second and third order of accuracy.

Likewise, the linear profiles in the faces of the zone in Fig. 1b only carry seven (not eight) independent pieces of information. (I.e., each face has a mean value and a slope, but the mean values are related via eqn. (3.1).) The magnetic field components in the right and left faces of Fig. 1b will also have piecewise linear slopes in the y-direction given by $B_y^{x\pm}$ respectively. Likewise, the magnetic field components in the top and bottom faces of Fig. 1b will also have piecewise linear slopes in the x-direction given by $B_x^{y\pm}$ respectively. Therefore, at the right and left faces of the reference element, the divergence-free reconstruction in the interior will have to match the two linear profiles for the x-component of the magnetic field given by

$$B^{x\pm}\left(y\right) = B_0^{x\pm} + B_y^{x\pm}\, y \tag{3.2}$$

Similarly, at the top and bottom faces of the reference element, the divergence-free reconstruction in the interior will have to match the two linear profiles for the y-component of the magnetic field given by

$$B^{y\pm}\left(x\right) = B_0^{y\pm} + B_x^{y\pm}\, x \tag{3.3}$$

We now turn our attention to the divergence-free reconstruction of the magnetic field in the interior of the zone shown in Fig. 1b.

We want the reconstructed magnetic field in the interior of the zone to be pointwise divergence-free everywhere within the zone. This *includes* the boundary of the zone. We therefore want the x-component of the magnetic field to match eqn. (3.2) at the right and left boundaries of the reference element. Furthermore, we want the y-component of the magnetic field to match eqn. (3.3) at the top and bottom boundaries of the reference element. If the polynomials used for the reconstruction are restricted to have linear variation, there are not enough degrees of freedom to match the seven independent pieces of boundary information. We, therefore, look for magnetic field profiles of the form

$$\begin{aligned} B^x(x,y) &= a_0 + a_x\, x + a_y\, y + a_{xx} \left(x^2 - 1/12\right) + a_{xy}\, x\, y \\ B^y(x,y) &= b_0 + b_x\, x + b_y\, y + b_{xy}\, x\, y + b_{yy} \left(y^2 - 1/12\right) \end{aligned} \tag{3.4}$$

Notice that each of the two above equations have two additional terms on the right hand side that go beyond simple linear variation. Maintaining a pointwise divergence-free condition anywhere within the zone then imposes three additional constraints on the coefficients in eqn. (3.4). The constraints that emerge from asserting $\partial_x B^x(x,y) + \partial_y B^y(x,y) = 0$ are:

$$2\, a_{xx} \;+\; b_{xy} \;=\; 0 \quad ; \quad a_{xy} \;+\; 2\, b_{yy} \;=\; 0 \quad ; \quad a_x \;+\; b_y \;=\; 0 \tag{3.5}$$

With these additional constraints, we see that the coefficients in eqn. (3.4) only have seven degrees of freedom which match exactly with the seven independent pieces of information represented by the linear profiles of the magnetic field components in the boundaries of the zone, see eqns. (3.2) and (3.3). Appendix A presents more information on exactly how the seven degrees of freedom for second order accurate reconstruction can be matched with the seven independent pieces of information represented by the linear profiles of the magnetic field components in the boundaries of the zone.

Appendix B describes the divergence-free reconstruction of magnetic fields at third order.

IV) Multidimensional Riemann Solvers for the Induction Equation

Fig. 2 shows the four states RU (right-up), LU (left-up), LD (left-down) and RD (right-down) that come together at a vertex of a two-dimensional Cartesian mesh. These four states contribute to the multidimensional Riemann problem at that vertex. (Such states are only shown for a few vertices in the figure. Each vertex will, of course, have different values for these four states.) The magnetic field $\left(B^x_{RU}, B^y_{RU}\right)$ in the RU state is obtained by applying the divergence-free reconstruction from the previous section to the zone that lies to the right-upper side of the vertex in question. The magnetic field $\left(B^x_{LU}, B^y_{LU}\right)$ in the LU state is obtained similarly from the zone that lies to the left-upper side of the vertex in question. The magnetic field $\left(B^x_{LD}, B^y_{LD}\right)$ in the LD state is obtained analogously from the left-down side of the vertex in question. The magnetic field $\left(B^x_{RD}, B^y_{RD}\right)$ in the RD state is also obtained similarly from the right-down side of the vertex in question. Please realize that the above four sentences describe magnetic fields that come from the four different zones that come together at the vertex. The multidimensional Riemann solver then gives us the z-component of the electric field at that vertex. Eqn. (1.1) can also be written in flux form. When that is done, the z-component of the electric field is given by the first component of the y-flux or the negative of the second component of the x-flux. These fluxes can be obtained from eqns. (12), (13) and (14) of Balsara [16].

For the simple problem associated with the induction equation it is not possible to endow any sub-structure to the multidimensional Riemann solver. As a result, the multidimensional Riemann solver can be obtained either by using the one-dimensional Lax-Friedrichs (LF) Riemann solver as a building block or by using the one-dimensional HLL Riemann solver as a building block. Both building blocks have their merits. They result in different multidimensional wave models with slightly different, though comparable, dissipation characteristics. We discuss each of these in the next two paragraphs along with the electric fields that they give rise to. Please note that even though the multidimensional Riemann solver uses four one-dimensional Riemann solvers, it is not a repeated application of one-dimensional Riemann solvers. The resolved state and fluxes coming from a multidimensional Riemann solver can be very different from the one-dimensional fluxes.

The one-dimensional LF Riemann solver has extremal speeds in the x-direction that are bounded by $-\left|\mathrm{v}_x\right|$ to $\left|\mathrm{v}_x\right|$. In the y-direction, the extremal speeds are bounded by $-\left|\mathrm{v}_y\right|$ to $\left|\mathrm{v}_y\right|$. As a result, the multidimensional Riemann solver that uses the one-dimensional LF Riemann solver as a building block will have a multidimensional wave model that has an extent of $\left[-\left|\mathrm{v}_x\right|,\left|\mathrm{v}_x\right|\right]\times\left[-\left|\mathrm{v}_y\right|,\left|\mathrm{v}_y\right|\right]$. For this multidimensional wave model, and for a given set of incoming states, eqns. (12), (13) and (14) of Balsara [16] will yield the multidimensionally upwinded fluxes. With a little rearrangement, the resulting electric field can be written as a centered part and a dissipation part. From the multidimensional LF Riemann solver we get the z-component of the electric field at a vertex as

$$\begin{aligned} E_{LF}^{z} = {} & \mathrm{v}_y \left(B_{RU}^{x} + B_{LU}^{x} + B_{LD}^{x} + B_{RD}^{x} \right) / 4 - \mathrm{v}_x \left(B_{RU}^{y} + B_{LU}^{y} + B_{LD}^{y} + B_{RD}^{y} \right) / 4 \\ & - \frac{\left|\mathrm{v}_y\right|}{2} \left(\left(B_{RU}^{x} + B_{LU}^{x} \right) / 2 - \left(B_{RD}^{x} + B_{LD}^{x} \right) / 2 \right) + \frac{\left|\mathrm{v}_x\right|}{2} \left(\left(B_{RU}^{y} + B_{RD}^{y} \right) / 2 - \left(B_{LU}^{y} + B_{LD}^{y} \right) / 2 \right) \end{aligned} \tag{4.1}$$

The first line in the above equation shows the centered electric field. The second line shows the dissipation terms. In order to bring out the multidimensional nature of the above equation, let us compare eqn. (4.1) to the canonical form of the one-dimensional LF flux for conservation laws. It is easy to see that the y-directional jump in the mean x-component of the magnetic field contributes to the dissipation term. Likewise, the x-directional jump in the mean y-component of the magnetic field also contributes to the dissipation term. Notice that eqn. (4.1) has a rather nice form where the dissipation can be truly multidimensional. For higher order schemes, the size of these jumps becomes smaller, resulting in reduced dissipation. The multidimensional HLL Riemann solver is described in detail in Appendix C. Eqns. (4.1) and (C.1) have been specialized for the induction equation with a constant velocity. When the velocity has piecewise variation within a zone, please use eqns. (12), (13) and (14) of Balsara [16] to obtain the multidimensional state and fluxes from the multidimensional Riemann solver. (The inclusion of substructure in those equations can be ignored.) Please also see Section VI of that same paper for implementation-related details. Eqns. (2) to (7) of Balsara [14] describe how the extremal speeds are derived for a multidimensional HLL Riemann solver on structured meshes. Please see the paragraph after eqn. (17) of Balsara [14] to understand how resetting the extremal speeds yields the multidimensional LLF Riemann solver. Eqn. (35) of Balsara [14] then describes how the z-component of the electric field is obtained from the multidimensional fluxes.

The multidimensional version of the LF Riemann solver, as well as the multidimensional version of the HLL Riemann solver, both have excellent multidimensional dissipation characteristics. This is made most apparent at first order accuracy. (I.e., when used without the higher order reconstruction, our multidimensional Riemann solver-based method becomes a first order accurate method that is amenable to the ensuing analytical treatment.) At first order, the divergence-free reconstruction is trivial. Also at first order, the electric field in eqn. (4.1) can be written explicitly by using the mesh function for the magnetic field components. We use the indexing of the mesh in Fig. 2 to write the electric field explicitly as

$$E^{z}_{LF;1/2,1/2} = \mathrm{v}_y \left(B^{x}_{1/2,1} + B^{x}_{1/2,0} \right) \big/ 2 - \mathrm{v}_x \left(B^{y}_{1,1/2} + B^{y}_{0,1/2} \right) \big/ 2 - \frac{\left|\mathrm{v}_y\right|}{2} \left(B^{x}_{1/2,1} - B^{x}_{1/2,0} \right) + \frac{\left|\mathrm{v}_x\right|}{2} \left(B^{y}_{1,1/2} - B^{y}_{0,1/2} \right) \quad (4.2)$$

The dissipation from the multidimensional LF Riemann solver is made even more apparent in the above equation. The first two terms show the centered electric field while the next two terms show the dissipation. In this very simple limit, eqn. (4.2) is just the CTU scheme by Colella [33].

An equation that is analogous to eqn. (4.2) can be written for $E^{z}_{LF;1/2,-1/2}$. Using eqn. (2.5a), we can now write an update equation for $B^{x}_{1/2,0}$. This is the magnetic field that is collocated in the right face of the (0,0) zone. After a little massaging of the resulting equation, and with the help of the discrete divergence condition, we get

$$\begin{aligned} \frac{dB^{x}_{1/2,0}}{dt} = &-\frac{\mathrm{v}_y}{2\Delta y}\left(B^{x}_{1/2,1}-B^{x}_{1/2,-1}\right)+\frac{\mathrm{v}_x}{\Delta y}\left(\left(B^{y}_{1,1/2}+B^{y}_{0,1/2}\right)/2-\left(B^{y}_{1,-1/2}+B^{y}_{0,-1/2}\right)/2\right) \\ &+\frac{\left|\mathrm{v}_x\right|}{2\Delta x}\left(B^{x}_{3/2,0}-2B^{x}_{1/2,0}+B^{x}_{-1/2,0}\right)+\frac{\left|\mathrm{v}_y\right|}{2\Delta y}\left(B^{x}_{1/2,1}-2B^{x}_{1/2,0}+B^{x}_{1/2,-1}\right) \end{aligned} \tag{4.3}$$

The first two terms on the right hand side of eqn. (4.3) clearly show the central form of the original PDE associated with the induction equation. The last two terms on the right hand side of eqn. (4.3) show the mesh-dependent parabolic dissipation associated with the multidimensional LF Riemann solver. Because of the presence of these parabolic terms, the multidimensional Riemann solver *always plays a stabilizing role* in the induction equation. The multidimensional HLL Riemann solver will of course show smaller levels of dissipation than the multidimensional LF Riemann solver, but it can also be reduced to a form that is entirely analogous to eqn. (4.3). These results do show substantial dissipation at first order, but at higher orders this large dissipation will be mostly mitigated by the higher quality reconstruction.

We also point out that the simple expressions in eqns. (4.1) and (C.1) are only a consequence of our very simple model problem, i.e. the induction equation. When the full MHD system is used, the structure of the multidimensional Riemann solver will be more complex. However, the essential insight that the multidimensional Riemann solver provides appropriate stabilization in multiple dimensions carries over.

V) von Neumann Stability Analysis of RKDG Schemes for the Induction Equation

Please realize that the induction equation is fundamentally multidimensional, so any meaningful von Neumann stability analysis should at least be two dimensional. Periodic boundary conditions are assumed for all the von Neumann stability work reported in this paper. In this section we show how such a stability analysis is carried out. In the next section we will present results from the von Neumann stability analysis of the induction equation. The von

Neumann stability analysis at first order can be carried out analytically which is why Sub-section V.1 is devoted to that task. At higher orders, i.e. for RKDG schemes with $P \geq 1$, one has to use a computer algebra system to carry out the von Neumann stability analysis at each different order. For this reason, Sub-section V.2 shows how such a stability analysis is carried out for P=1 RKDG schemes. Once the general principle is understood, it can be extended to even higher orders.

The two-dimensional von Neumann stability analysis that we present here is restricted to a constant velocity vector $\mathbf{v} = \mathrm{v}_x \hat{x} + \mathrm{v}_y \hat{y}$ and a uniform mesh with zone sizes Δx and Δy in the x- and y-directions. We also restrict our focus to a linear RKDG scheme, i.e. one that does not incorporate limiters. Von Neumann stability analysis forces us to restrict our focus to linear RKDG schemes and previous work on the RKDG schemes for scalar advection (Zhang and Shu [52], Liu *et al*. [41]) was also similarly restricted.

V.1) von Neumann Stability Analysis of the First Order (i.e., P=0) RKDG Scheme

The first order RKDG scheme (P=0) corresponds to a standard finite volume scheme, where only averaged quantities are updated. For the present scheme, these would only be the facially averaged magnetic field components. At first order the problem can be solved analytically. It consists of realizing that the second term on the right hand side of eqn. (4.3) can be rewritten exclusively in terms of the x-components of the magnetic field if the discrete divergence free condition from eqn. (3.1) is used. In other words, realize that we can write $\left(B^y_{0,1/2} - B^y_{0,-1/2}\right) = -\left(B^x_{1/2,0} - B^x_{-1/2,0}\right)\Delta y/\Delta x$ and analogous expressions in the other zones. Thus eqn. (4.3) becomes

$$\begin{aligned}\frac{dB^x_{1/2,0}}{dt} = &-\frac{\mathrm{v}_y}{2\Delta y}\left(B^x_{1/2,1} - B^x_{1/2,-1}\right) - \frac{\mathrm{v}_x}{2\Delta x}\left(B^x_{3/2,0} - B^x_{-1/2,0}\right) \\ &+\frac{\left|\mathrm{v}_x\right|}{2\Delta x}\left(B^x_{3/2,0} - 2B^x_{1/2,0} + B^x_{-1/2,0}\right) + \frac{\left|\mathrm{v}_y\right|}{2\Delta y}\left(B^x_{1/2,1} - 2B^x_{1/2,0} + B^x_{1/2,-1}\right)\end{aligned} \qquad (5.1)$$

Observe now that eqn. (5.1) is still a multidimensional equation for the time evolution of $B^x_{1/2,0}$. However, it is an advection diffusion equation that is written entirely in terms of the x-component of the magnetic field. The diffusion terms are of course dependent on the mesh size and tend to zero as the mesh becomes finer and finer. In practice, the amount of diffusion imparted by our Riemann solver-based scheme also depends on whether the magnetic field has a smooth variation on the computational mesh or whether it has local discontinuities. It is, however, very instructive to show that the use of the multidimensional Riemann solver gives us an update that can be written as a centered update plus a diffusive part, which is always stabilizing in a fully multidimensional sense. An analogous equation can be written for the time-evolution of the y-component of the magnetic field and is given by

$$\begin{aligned}\frac{dB^y_{0,1/2}}{dt} = &-\frac{\mathrm{v}_x}{2\Delta x}\left(B^y_{1,1/2} - B^y_{-1,1/2}\right) - \frac{\mathrm{v}_y}{2\Delta y}\left(B^y_{0,3/2} - B^y_{0,-1/2}\right) \\ &+ \frac{\left|\mathrm{v}_x\right|}{2\Delta x}\left(B^y_{1,1/2} - 2B^y_{0,1/2} + B^y_{-1,1/2}\right) + \frac{\left|\mathrm{v}_y\right|}{2\Delta y}\left(B^y_{0,3/2} - 2B^y_{0,1/2} + B^y_{0,-1/2}\right)\end{aligned} \qquad (5.2)$$

This simplification only obtains at first order when the discrete divergence condition holds. At higher orders, we do not get any analogous simplification.

Endowing the x-component of the magnetic field with Fourier dependence, we can use eqn. (5.1) to obtain the amplification factor of the scheme after one first order accurate timestep. Requiring the amplification factor of the scheme to be bounded by unity, we get the CFL condition:-

$$\left|\frac{\mathrm{v}_x \Delta t}{\Delta x}\right| + \left|\frac{\mathrm{v}_y \Delta t}{\Delta y}\right| \le 1 \qquad (5.3)$$

Please realize that at first order the discrete divergence-free condition relates the Fourier coefficients of the x-component of the magnetic field to the Fourier coefficients of the y-component of the magnetic field. As a result, no separate Fourier analysis is needed for the y-component of the magnetic field.

V.2) von Neumann Stability Analysis of the Second Order (i.e., P=1) RKDG Scheme

Expressed in terms of moments, each face of the mesh will have a mean magnetic field component and its slope along the face when the P=1 RKDG discretization is used. Thus each face carries two pieces of information, which can equivalently be mapped to two nodal values for the magnetic field component that resides in that face. Please see Fig. 2 which shows the nodal points as well as the magnetic field components associated with those nodes for the zone (0,0). The nodal locations are chosen to be the Gauss-Legendre quadrature points. (Other quadrature points were tried but did not seem to make a difference in the stability analysis.) Thus the right face for the zone (0,0) has two nodal values B_{n1}^{x} and B_{n2}^{x} for the x-component of the magnetic field. The left face of the same zone has two nodal values B_{n3}^{x} and B_{n4}^{x} for the x-component of the magnetic field. Our von Neumann analysis is carried out in terms of Fourier modes. The modes have spatial dependence of the form $e^{i\left(k_x x+k_y y\right)}$ with wave numbers k_x and k_y on a uniform mesh with zones of size Δx and Δy. Because we use periodic boundary conditions, the nodal values in the right and left faces of the zone (0,0) are related by the phase shifts

$$B_{n3}^{x}=B_{n1}^{x}e^{-ik_x\Delta x} \quad ; \quad B_{n4}^{x}=B_{n2}^{x}e^{-ik_x\Delta x} \tag{5.4}$$

The top face of the zone (0,0) has two nodal values B_{n1}^{y} and B_{n2}^{y} for the y-component of the magnetic field. The bottom face of the same zone has nodal values B_{n3}^{y} and B_{n4}^{y} for the y-component of the magnetic field. Again, the nodal values are related by the phase shifts

$$B_{n3}^{y}=B_{n1}^{y}e^{-ik_y\Delta y} \quad ; \quad B_{n4}^{y}=B_{n2}^{y}e^{-ik_y\Delta y} \tag{5.5}$$

We incorporate eqns. (5.4) and (5.5) in the discrete divergence-free condition. The discrete divergence-free condition applied to zone (0,0) then enables us to write

$$B_{n2}^{y}=-B_{n1}^{y}-\frac{\Delta y}{\Delta x}\frac{1-e^{-ik_x\Delta x}}{1-e^{-ik_y\Delta y}}\left(B_{n1}^{x}+B_{n2}^{x}\right) \tag{5.6}$$

We easily see that, with the discrete divergence-free condition incorporated from eqn. (3.1), and also with the phase shifts from eqns. (5.4) and (5.5), we have obtained a significant simplification in eqn. (5.6). For the sake of clarity, let us amplify the previous sentence a little further. The x-component of the magnetic field in the right face of zone (0,0) is given by $B_{0;1/2,0}^{x}=\left(B_{n1}^{x}+B_{n2}^{x}\right)/2$. Because of condition (5.4), the x-component of the magnetic field in the left face is then given by $B_{0;-1/2,0}^{x}=\left(B_{n1}^{x}+B_{n2}^{x}\right)e^{-ik_x\Delta x}/2$. Use of eqn. (5.5) shows us that a similar consideration applies to the y-components of the magnetic fields in upper and lower faces of zone (0,0). The discrete divergence-free condition in eqn. (3.1) then gives us eqn. (5.6). The independent nodal values within zone (0,0) are simply B^x_{n1} , B^x_{n2} and B^y_{n1}. The nodal value B^y_{n2} is not independent because it is related to B^x_{n1} , B^x_{n2} and B^y_{n1} via eqn. (5.6). All of the other magnetic field components at all of the nodes shown in Fig. 2 can be related to B^x_{n1} , B^x_{n2} and B^y_{n1} with phase shifts that are analogous to eqns. (5.4) and (5.5). The discussion in this paragraph, therefore, provides the stage setting for the von Neumann stability analysis.

Observe something interesting about Fig. 2. The nodes shown in Fig. 2 are indeed the only nodes that will contribute to the time-update of the magnetic fields that reside in the faces of the zone (0,0). Thus Fig. 2 shows us the full stencil of zones that contribute to zone (0,0). However, the unfilled nodes in Fig. 2 finally drop out of the final von Neumann stability analysis as will be discussed in the end of this Sub-section. In each of those nine zones, we can relate the nodal values of the magnetic field components to their modal values. Assuming Gauss-Legendre quadrature, this can be explicitly done for the right face of zone (0,0) as

$$B^x_{0;1/2,0} = \left(B^x_{n1} + B^x_{n2}\right)\big/2 \quad ; \quad B^x_{y;1/2,0} = \left(B^x_{n2} - B^x_{n1}\right)\sqrt{3} \tag{5.7}$$

In the above equation, $B^x_{0;1/2,0}$ is the mean x-component of the magnetic field in the (1/2,0) face shown in Fig. 2 and $B^x_{y;1/2,0}$ is the linear variation (i.e., y-directional slope) for the same magnetic field component in the same face. Similarly, for the upper face of zone (0,0) we have

$$B^y_{0;0,1/2} = \left(B^y_{n1} + B^y_{n2}\right)\big/2 \quad ; \quad B^y_{x;0,1/2} = \left(B^y_{n2} - B^y_{n1}\right)\sqrt{3} \tag{5.8}$$

In the above equation, $B^y_{0;0,1/2}$ is the mean y-component of the magnetic field in the (0,1/2) face shown in Fig. 2 and $B^y_{x;0,1/2}$ is the linear variation (i.e., x-directional slope) for the same magnetic field component in the same face. With these mean values and slopes specified, we can make the divergence-free reconstruction from Section III in each of the nine zones shown in Fig. 2. The reconstruction depends only linearly on the facial values and their slopes. Using the Fourier dependence from equations like eqn. (5.4) and (5.5), the divergence-free reconstruction in each of the nine zones of Fig. 2 can be expressed exclusively in terms of B^x_{n1} , B^x_{n2} and B^y_{n1}. This is where we have to rely on the strong capabilities of modern computer algebra systems. We used the Mathematica and Macsyma computer algebra systems.

A glance at the update equations (2.5) and (2.7) shows that we will need the electric fields at the vertices and also the electric fields at the nodal points within each face. Let us first focus on the electric fields at the vertices. Specifically, let us focus on the vertex of the zone (0,0) that lies North-East of the zone center in Fig. 2. Divergence-free reconstruction within the (1,1) zone can be used to find $\left(B_{RU}^x, B_{RU}^y\right)$. An analogous process in the (0,1) zone can be used to find $\left(B_{LU}^x, B_{LU}^y\right)$. Similarly, the (0,0) zone can be used to find $\left(B_{LD}^x, B_{LD}^y\right)$. In the same way, (1,0) zone can be used to find $\left(B_{RD}^x, B_{RD}^y\right)$. These are the four states that can be input into the multidimensional Riemann solver to get the z-component of the electric field; see eqns. (4.1) or (C.1). Also recall that all these four states described above can be expressed exclusively in terms of B_{n1}^x , B_{n2}^x and B_{n1}^y using a computer algebra system. As a result, the z-components of the electric field at all of the vertices of the zone (0,0) shown in Fig. 2 can be expressed exclusively in terms of B_{n1}^x , B_{n2}^x and B_{n1}^y. Modern computer algebra systems are powerful enough to handle this mathematics precisely.

We now switch focus to obtaining the z-component of the electric field within each zone boundary for the zone (0,0) in Fig. 2. These electric fields are needed for the angled brackets in eqns. (2.5b) and (2.7b). To get the electric fields at the two nodes in the right face of the (0,0) zone, we solve the x-directional Riemann problem at those two nodes. The left state at either of those two nodes is obtained from the divergence-free reconstruction in zone (0,0). The right state at either of those two nodes is obtained from the divergence-free reconstruction in zone (1,0). Notice that while the x-component of the magnetic field will be continuous across that right face, the y-component of the magnetic field can indeed have a jump in it. That jump is crucial for introducing dissipation that stabilizes the scheme. (Let us consider the simple example for the one-dimensional LLF Riemann solver which is applied in the x-direction. Let the left state have magnetic field vector $B_L^x \hat{x} + B_L^y \hat{y}$ and let the right state have magnetic field vector $B_R^x \hat{x} + B_R^y \hat{y}$. The resolved magnetic field vector $B^{x*} \hat{x} + B^{y*} \hat{y}$ at the zone boundary is just $\frac{1}{2}\left(B_L^x + B_R^x\right)\hat{x} + B_L^y \hat{y}$

if $\mathrm{v}_x \geq 0$ and $\frac{1}{2}\left(B_L^x + B_R^x\right)\hat{x} + B_R^y\hat{y}$ if $\mathrm{v}_x < 0$. The corresponding z-component of the electric field at the zone boundary is given by $\mathrm{v}_y B^{x*} - \mathrm{v}_x B^{y*}$.) The electric fields at the other nodal points within the zone (0,0) are obtained similarly. They can all be expressed exclusively in terms of B_{n1}^x , B_{n2}^x and B_{n1}^y. Again, modern computer algebra systems are powerful enough to handle this mathematics precisely.

Once the z-component of the electric field is obtained at the vertices of the mesh as well as the facial nodal points, we are ready to evaluate the time rates of change shown in eqns. (2.5a), (2.5b), (2.7a) and (2.7b). If we focus on the right face and the upper face of zone (0,0) in Fig. 2, we can obtain the time rates of update for the magnetic field components that are collocated to the nodes within those two faces. Operationally, this is done as follows. Eqn. (2.5a) gives us $dB_{0;1/2,0}^x \big/ dt$. Eqn. (2.5b) gives us $dB_{y;1/2,0}^x \big/ dt$. Differentiating eqn. (5.7) with respect to time then allows us to obtain

$$\frac{dB_{n1}^x}{dt} = \frac{dB_{0;1/2,0}^x}{dt} - \frac{1}{2\sqrt{3}}\frac{dB_{y;1/2,0}^x}{dt} \quad ; \quad \frac{dB_{n2}^x}{dt} = \frac{dB_{0;1/2,0}^x}{dt} + \frac{1}{2\sqrt{3}}\frac{dB_{y;1/2,0}^x}{dt} \tag{5.9}$$

Eqn. (2.7a) gives us $dB_{0;0,1/2}^y \big/ dt$. Eqn. (2.7b) gives us $dB_{x;0,1/2}^y \big/ dt$. Eqn. (5.8) then allows us to obtain

$$\frac{dB_{n1}^y}{dt} = \frac{dB_{0;0,1/2}^y}{dt} - \frac{1}{2\sqrt{3}}\frac{dB_{x;0,1/2}^y}{dt} \quad ; \quad \frac{dB_{n2}^y}{dt} = \frac{dB_{0;0,1/2}^y}{dt} + \frac{1}{2\sqrt{3}}\frac{dB_{x;0,1/2}^y}{dt} \tag{5.10}$$

Now please realize that within the context of a von Neumann stability analysis that is based on Fourier modes, the right hand sides of eqns. (5.9) and (5.10) are exclusively dependent on the three nodal values B_{n1}^x , B_{n2}^x and B_{n1}^y. Let us, therefore, pick the two equations in eqn. (5.9) and the first equation in eqn. (5.10). The time rates of update can be formally written as

$$\begin{aligned}
\frac{dB^x_{n1}}{dt} &= A_{11}B^x_{n1} + A_{12}B^x_{n2} + A_{13}B^y_{n1} \\
\frac{dB^x_{n2}}{dt} &= A_{21}B^x_{n1} + A_{22}B^x_{n2} + A_{23}B^y_{n1} \\
\frac{dB^y_{n1}}{dt} &= A_{31}B^x_{n1} + A_{32}B^x_{n2} + A_{33}B^y_{n1}
\end{aligned} \qquad (5.11)$$

The nine coefficients on the right hand side of eqn. (5.11) form a 3×3 matrix, which we call "**A**". Those coefficients only depend on the velocity components v_x and v_y , the zone sizes Δx and Δy and the wave numbers k_x and k_y. Appendix D explicitly catalogues the nine coefficients on the right hand side of eqn. (5.11). It will enable interested readers to cross-check their implementations in their computer algebra systems versus ours. Also note that eqn. (5.11), along with the extra information from Appendix D, can be used as a semi-discrete von Neumann (mode) analysis of the spatial operator independent of the time discretization in a so-called method-of-lines approach. The spectrum of this discrete spatial operator might be useful in its own right, and any follow-on researchers would then be able to apply their chosen time discretization method to eqn. (5.11).

Taken by itself, eqn. (5.11) provides a continuous in time but second order discrete in space von Neumann stability analysis of the induction equation. However, it can be coupled to a suitable RK2 scheme to obtain the amplification matrix of an RKDG scheme that is second order in space and second order in time. Use of a suitable RK3 scheme provides the amplification matrix of an RKDG scheme that is second order in space and third order in time. This process can be continued to get a sequence of RKDG schemes that are second order in space and at least second order accurate in time. The stability properties of such schemes will be analyzed in detail in the next section.

It is also useful to make a special note about the stencil depicted in Fig. 2. Only the filled nodal points truly contribute to the update of the nodal points that lie on the faces of the (0,0) zone. There are some further unfilled nodal points shown in zones (1,1), (-1,1), (-1,-1) and (1,-1). They can be used to simplify the divergence-free calculation procedure, but they eventually drop out of the von Neumann stability calculation. Thus the entire von Neumann stability analysis only relies on the nodal points that reside on the faces of zones (0,0), (1,0), (-1,0), (0, 1) and (0,-

1). In that sense, the von Neumann stability analysis described here truly pertains to a RKDG scheme with the smallest stencil possible.

While the present section has only studied the P=1 RKDG schemes, the process can be extended to RKDG schemes with $P \geq 1$. For $P \geq 3$ we found that the computer algebra system itself couldn't perform the simplifications that were needed to keep the solution procedure tractable. In other words, DG discretizations that are up to third order accurate in space have been analyzed in this paper and we report on them in the next section. For $P \geq 3$ the divergence-free reconstruction is not uniquely defined by the normal component of the magnetic field. However, least squares minimization, as described in Balsara [7] or Balsara and Dumbser [20], is sufficient to yield uniquely defined magnetic fields. This least squares minimization is equivalent to minimizing the magnetic energy, or equivalently, minimizing the variation in the magnetic field. The resulting schemes preserve the desired order of accuracy.

VI) Results from the von Neumann Stability Analysis of RKDG Schemes

A von Neumann stability analysis, especially one that is done for a full scheme in two-dimensions, can give us a wealth of information. The most important information corresponds to the stability limit of the Runge-Kutta timestepping strategy; i.e. the largest possible CFL number of the scheme. This is displayed in Sub-section VI.a for RKDG schemes for the induction equation at first, second and third orders of accuracy. We can also use von Neumann stability to study the isotropic propagation of wave modes in all directions on a computational mesh. This is presented in Sub-section VI.b. Once a stable algorithm has been documented, we can also use von Neumann stability analysis to evaluate the stability of various variants upon the basic algorithm. In other words, we ask:- Even if it is possible to obtain simpler divergence-free RKDG schemes for the induction equation, are they all stable? This question is addressed in Sub-section VI.c.

VI.a) Stable CFL Numbers for Divergence-free RKDG Schemes for the Induction Equation

Fig 3 shows the domain of stability for the first order (P=0) DG scheme with forward Euler timestepping. The x- and y-axes of the plot show the CFL number in the x- and y-directions. In other words, the axes display the *x*- and *y*-directional Courant numbers given by

$C_x \equiv |\mathrm{v}_x| \Delta t / \Delta x$ and $C_y \equiv |\mathrm{v}_y| \Delta t / \Delta y$. For our purposes, the multidimensional CFL number that is used all through this paper is defined by $\sqrt{C_x^2 + C_y^2}$. The CFL number is just the radius of the largest circle (in the Euclidean norm) remaining within the stability region in the ensuing Figs. 3, 4 and 5. For the stability analysis presented in this paper, the mesh is Cartesian with $\Delta x = \Delta y$. (In practice, the ratio $\Delta y / \Delta x$ can always be absorbed in the definition of the x- and y-directional CFL numbers.) The color in Fig. 3 shows the maximum amplitude of the amplification factor over all wave modes. The white lines identify the boundary of the domain of stability; i.e., where the amplification factor reaches unity. Within the domain of stability, the amplification factor is less than or equal to unity for all possible wave modes that can propagate on the mesh. Notice that the domain of stability exactly matches the prediction from eqn. (5.3).

Operationally, Fig. 3 was obtained from a computer code that divided the domain shown in the plot into little cells, or pixels. Each such cell corresponds to an *x*-directional and a *y*-directional CFL number. (Thus the choice of a specific *x*-directional and *y*-directional CFL number is tantamount to choosing an *x*-directional and a *y*-directional velocity.) For each such cell we evaluated the amplification factor for wave modes $(k_x \Delta x, k_y \Delta y) \in [-\pi/2, \pi/2] \times [-\pi/2, \pi/2]$. In practice, the full range of CFL numbers are discretized by 401^2 cells and the full range of wave modes is also discretized by 401^2 cells. In general the amplification factor is a complex number. The maximum absolute value from that scan was then colorized and plotted out for each pixel/cell. The result is shown in Fig. 3 which gives us a very clear visual understanding of the stability of the scheme. Unless stated otherwise, all figures in this section correspond to the use of a LF flux in one and two-dimensions.

Fig. 4 shows the domain of stability for the second order (P=1) DG scheme with several different timestepping strategies. Figs. 4a and 4b show the result of using the second and third order SSP schemes from Shu and Osher [90]. Fig. 4c shows the result of using the RK(5,4) scheme from Spiteri and Ruuth [46] which is also documented in Gottlieb [38]. RK(5,4) is a five-stage, fourth-order accurate in time SSP Runge-Kutta scheme with some very enhanced stability properties, which is why we chose it for our default fourth order accurate in time Runge-Kutta scheme. The white curves identify the boundary of the domain of stability. Please recall that the matrix "$\mathbf{A}$" from eqn. (5.11) is a 3×3 matrix. The resulting scheme, with a Runge-

Kutta timestepping, will also produce a 3×3 matrix whose complex eigenvalues can then be evaluated by a computer program. For von Neumann stability analysis, we are interested in the eigenvalue with the largest amplitude. This largest amplitude was colorized and displayed in Fig. 4. Comparing Figs. 4a and 4b we clearly see that the three-stage scheme permits a better CFL number. Focusing on Fig. 4c we can also see that the RK(5,4) scheme shows its worth by permitting a much larger domain of stability. It is important to realize that this stability analysis is truly two-dimensional and the boundaries of the stability domain indeed show the effect of mesh imprinting. We will have more to say about the important topic of mesh imprinting in the next Sub-section. We also mention that when forward Euler timestepping is used, the P=1 DG scheme is unstable; a result that is unsurprising given the findings of Cockburn and Shu [31], Zhang and Shu [52] and Liu *et al*. [41]. Please also see Table 2.2 from Cockburn and Shu [31].

Fig. 5 shows the domain of stability for the third order (P=2) DG scheme with several different Runge-Kutta timestepping strategies. Fig. 5a shows the result of using the third order SSP scheme from Shu and Osher [90]. Fig. 5b shows the result of using the RK(5,4) scheme. Again we see that the RK(5,4) scheme offers much-improved stability properties. We also mention that with first or second order Runge-Kutta timestepping the P=2 DG scheme is unstable at fixed CFL number, which also reflects the results from Cockburn and Shu [31].

The plots shown in Figs. 3 to 5 enable us to make a table that is suitable for practical use. Recall that the CFL number is just the radius of the largest circle (in the Euclidean norm) remaining within the stability region in Figs. 3, 4 and 5. Table I shows the maximal CFL number for DG schemes with various orders of spatial accuracy that are used in conjunction with Runge-Kutta schemes with various orders of temporal accuracy. A dash in Table I indicates that the scheme is unstable. Observe that the limiting CFL in Table I is very compatible with the limiting CFLs for DG schemes from Cockburn and Shu [31]. Please see Table 2.2 from Cockburn and Shu [31]. Recall that the limiting CFL analysis of Cockburn and Shu [31] is strictly one-dimensional. When the flow becomes mesh-aligned, it is not possible to have a CFL that is better than the one-dimensional one. I.e. while the induction equation is truly multidimensional, it is indeed the one-dimensional effects that set the CFL. This suggests that a full-fledged RKDG scheme for divergence-free MHD will have CFL numbers that are competitive with its Euler counterparts. This bodes well for the construction of divergence-free

RKDG schemes for MHD. Also notice that the classical RK4 scheme has a limiting CFL number that is substantially lower than the SSP-RK(5,4) timestepping scheme. This is consistent with expectations because SSP-RK(5,4) incorporates an extra stage and has been designed to have a large CFL.

All the previously-mentioned results in this Sub-section were for electric fields that are evaluated using an LF Riemann solver in one- and two-dimensions. The electric field from the multidimensional LF Riemann solver is explicitly catalogued in eqn. (4.2). An analogous equation can be written for the multidimensional HLL Riemann solver; see eqn. (C.1). Also recall that our analysis for the multidimensional HLL Riemann solver will be done with $c_x = 1.2\ |\mathrm{v}_x|$ and $c_y = 1.2\ |\mathrm{v}_y|$; i.e., with "magnetosonic" signal speeds that are 20% larger than the velocity. There is no need to repeat the details here because the overall finding is indeed the expected one – the effective CFL number (evaluated w.r.t. velocities) is reduced by 20%. This makes sense because the overall timestep in a code goes down as the maximum signal speed is increased. If we were to plot figures for the multidimensional HLL Riemann solver that are analogous to Figs. 3, 4 and 5, the resulting figures would indeed look entirely similar to the original figures with a 20% scale reduction. For that reason, we do not repeat such figures in this paper.

Table I shows the limiting CFL number for a large number of possible RKDG schemes. The table shows spatial order of accuracy of DG schemes in the horizontal direction and temporal order of accuracy of the Runge-Kutta timestepping in the vertical direction. The CFL number is just the radius of the largest circle remaining within the stability region in figures 3, 4 and 5.

	P=0	P=1	P=2
RK1	0.7071	______	______
SSP-RK2	0.7071	0.3161	______
SSP-RK3	0.8883	0.3904	0.2069
RK4 (classical)	0.9846	0.4404	0.2318
SSP-RK(5,4)	1.5490	0.6366	0.3400
RK5 (classical)	1.1372	0.5079	0.2676

VI.b) Analyzing the Isotropic Propagation of Wave Modes for RKDG Schemes

We wish to study the wave propagation characteristics of RKDG schemes for the induction equation. Any scheme will permit the longest wave length (smallest wave number) modes to propagate with minimal damping. A better scheme should permit more modes to propagate with minimal damping. While the accuracy of a scheme is related to the accuracy of the amplification factor at small wave numbers, it is desirable to have an amplification factor that is close to unity for a larger range of small wave numbers. Ideally, we would like to see a situation where higher order schemes permit a larger range of long wave length (small wave number) modes to propagate nearly undamped in all possible directions on a two-dimensional computational mesh. Given the von Neumann stability analysis that we have constructed, this is easy to demonstrate. Operationally, we choose a direction for the velocity vector. (The magnitude of the velocity vector is set by the choice of CFL number. The directions of the velocity vector will be specified in the next paragraph when the figures are discussed.) For that direction of the velocity, we can obtain the full range of amplification factors for wave numbers in the range $\left(k_x\Delta x, k_y\Delta y\right)\in\left[-\pi/2,\pi/2\right]\times\left[-\pi/2,\pi/2\right]$. This aforementioned range of wave numbers allows us to examine all the wave modes that have all possible *orientations* on the mesh. A scatterplot is then made of the amplification factor as a function of $\Delta x\sqrt{k_x^2+k_y^2}$. Each choice of $\sqrt{k_x^2+k_y^2}$ picks out several pairs of wave modes $\left(k_x,k_y\right)$ that have all possible orientations with respect to the mesh. Since RKDG schemes are operated close to their maximum CFL number, we choose a CFL that is 80% of the maximal CFL number from Table I.

Figs. 6a, 6b, 6c and 6d show the result of such a wave propagation study when the velocity vector makes angles of 0°, 15°, 30° and 45° to the mesh for the second order (P=1) DG scheme with SSP-RK2. Figs. 7a, 7b, 7c and 7d show the result of such a wave propagation study when the velocity vector makes angles of 0°, 15°, 30° and 45° to the mesh for the third order (P=2) DG scheme with SSP-RK3. (Please recall that in our model problem the velocity vector sets the direction of the advection of the magnetic fields but the wave numbers determine the orientation of the waves with respect to the mesh. The wave numbers also determine the ratio of the wavelength of the waves with respect to the mesh size.) We expect the reader to intercompare Figs. 6 and 7; consequently, the amplification factors for these two figures have the same vertical scale. We see that as the accuracy of the RKDG scheme increases, its ability to isotropically propagate wave modes is also increased. For example, the smallest amplification factors for the second order scheme in Figs. 6a, 6b, 6c and 6d lie between 0.6 to 0.8. Also notice that several short wavelength modes in Fig. 6 have amplification factors that are in that range. By contrast, all of the wave modes for the third order scheme in Figs. 7a, 7b, 7c and 7d have amplification factors that are larger than 0.8. Also notice that many of the long wavelength modes in Fig. 7 have amplification factors that are indeed quite close to unity.

In all instances we see that wave modes which are close to the Nyquist limit of the mesh are indeed damped; i.e, they have amplification factors that are less than unity. This is essential if the numerical method is to remain stable. (The Nyquist limit on a mesh corresponds to waves with a wavelength of just two mesh zones.)

VI.c) Is it Possible to have Simpler Divergence-free RKDG Schemes for the Induction Equation?

As one can see from Section III, the divergence-free reconstruction entails a few more terms that are required to make the method globally divergence-free. It is, therefore, natural to ask, “Is it possible to have simpler divergence-free RKDG schemes for the induction equation?”. In this Sub-section we focus on the two most natural simplifications that one might seek out and show that in each instance the simplification results in a linearly unstable divergence-free RKDG scheme. The two natural “simplifications” consist of:- a) simplifying the divergence-free reconstruction and b) the use of centered fluxes instead of upwinded fluxes wherever possible. We show below that either of the simplifications result in unstable schemes.

The first and most natural instinct is to try and simplify the reconstruction. For example, it is very natural to imagine the following second order, piecewise linear reconstruction of the magnetic field which is not globally divergence-free:

$$
\begin{aligned}
B^x(x,y) &= a_0 + a_x\, x + a_y\, y \\
&\qquad \text{with } a_0 = \left(B_0^{x+} + B_0^{x-}\right)\big/2 \;;\; a_x = B_0^{x+} - B_0^{x-} \;;\; a_y = \left(B_y^{x+} + B_y^{x-}\right)\big/2 \\
B^y(x,y) &= b_0 + b_x\, x + b_y\, y \\
&\qquad \text{with } b_0 = \left(B_0^{y+} + B_0^{y-}\right)\big/2 \;;\; b_x = \left(B_x^{y+} + B_x^{y-}\right)\big/2 \;;\; b_y = B_0^{y+} - B_0^{y-}
\end{aligned}
\tag{6.1}
$$

Here $B_0^{x\pm}$, $B_0^{y\pm}$, $B_y^{x\pm}$ and $B_x^{y\pm}$ are defined exactly as in eqns. (3.2) and (3.3); consequently, the syncopated reconstruction in eqn. (6.1) is fully specified. While this reconstruction will be *locally* divergence-free within the zone of interest because it satisfies $a_x + b_y = 0$, it will indeed produce jumps in the longitudinal component of the magnetic field at each boundary. Thus it is not *globally* divergence-free. The most natural resolution is to take the arithmetic average of the longitudinal magnetic field at each zone boundary. For the P=1 DG scheme described in this paragraph, we carried out a von Neumann stability analysis and found it unstable. Indeed, it was unstable with SSP-RK2, SSP-RK3 and SSP-RK(5,4), showing that it was unequivocally unstable. To bolster this finding, we constructed a P=2 DG scheme for the induction equation that was again not globally divergence-free and we found it to be unstable.

An examination of eqns. (2.5b) and (2.7b) suggests a second simplification to the P=1 DG scheme for the induction equation. We recognize of course that the electric fields at the vertices of the mesh should be obtained from the two-dimensional Riemann solver. However, it is natural to ask, “Can we simplify the evaluation of the angled brackets in those two equations? I.e., can we use a centered flux instead of an upwinded LF or HLL flux in the angled brackets of those two equations?” The answer from von Neumann stability analysis is an unequivocal negative! As before, we also experimented with making similar simplifications for the P=2 DG scheme for the induction equation and that too turned out to be unstable.

Based on these attempted simplifications we claim that the DG scheme described in Sections II, III and IV represents an absolute minimum set of algorithms that should be used in a divergence-free DG formulation of the induction equation.

VII) Accuracy analysis for RKDG and PNPM Schemes for the Induction Equation

In this section, we present numerical accuracy analyses of the RKDG schemes designed here. The third order RKDG scheme can also be thought of as a P2P2 scheme. It is, therefore, interesting to also analyze the numerical accuracy of P0P2 and P1P2 schemes and compare them with the P2P2 scheme. The P0P2 scheme is just a third order WENO scheme where the first and second moments within each face were reconstructed. The P1P2 scheme evolves the first moment while reconstructing the second moment in WENO fashion; i.e. the P1P2 scheme is basically a third order HWENO scheme. The P0P2 scheme has the advantage that it can be run with a CFL number that is comparable to that of a P=0 DG scheme. The P1P2 scheme can be run with a CFL number that is comparable to that of a P=1 DG scheme. For that reason, the P0P2 and P1P2 schemes offer a substantial timestep advantage over the third order RKDG scheme.

VII.1) Plane Wave Test Problem

This plane wave test problem is run on a uniform Cartesian mesh spanning $\left[-0.5,0.5\right]\times\left[-0.5,0.5\right]$ with periodic boundary conditions. We use $\mathrm{v}_x = \mathrm{v}_y = 1$. The magnetic field is set up by using a vector potential approach. The vector potential, as well as its time-evolution, are given by

$$\mathbf{A}\left(x,y,t\right) = \mathbf{z}\cos\left(k_x x + k_y y - \mathrm{v}_x k_x t - \mathrm{v}_y k_y t\right)$$

For the present test problem, we use $k_x = k_y = 2\pi$. The *x*- and *y*-components of the magnetic field are then given by

$$B_x = \frac{\partial A_z}{\partial y} \quad ; \quad B_y = -\frac{\partial A_z}{\partial x}$$

Because the solution is analytical, the accuracy of the error in the computed solution can be evaluated at any time. The accuracy is evaluated at a unit time.

Table II and III show the accuracy analyses for the P=1 and P=2 RKDG schemes. Both schemes meet their design accuracies in L_1 and L_∞ norms. We see that the P=2 RKDG is definitely superior to the P=1 RKDG scheme. The tables also show the total magnetic energy on the mesh as a fraction of the initial magnetic energy. We see that when there are about sixteen zones per wavelength, at least 96% of the total magnetic energy is retained by the simulation. On the finer meshes, the P=2 DG scheme is almost two orders of magnitude more accurate than the P=1 DG scheme. This shows the great value of higher order accurate DG schemes.

In Tables IV and V we show the accuracy analysis for the P0P2 and P1P2 schemes. The P0P2 scheme is basically a centered, third order WENO scheme. The P1P2 scheme can also be referred to as an HWENO scheme. We see that the P0P2 scheme shows some obvious deficiencies relative to the P=2 DG scheme. The P0P2 scheme is not as accurate as the P=2 DG scheme at all mesh resolutions, though it does meet its design accuracy. The P0P2 scheme also does not retain as much of the magnetic energy by the end of the simulation. The P0P2 scheme reconstructs all the moments of the magnetic field at every timestep and, consequently, accuracy as well as the retention of the magnetic energy are inferior. Turning now to the P1P2 scheme, we see that its accuracy is entirely comparable to the P=2 DG scheme. Furthermore, it retains the magnetic energy on the mesh very nicely. Thus the P1P2 scheme is almost comparable to the P=2 DG scheme in all respects; however the P1P2 scheme permits us to take substantially larger timesteps. This suggests that retaining the lower moments is crucial to improving accuracy; but the higher moments may not be as important at retaining accuracy. The larger permissible timestep of the P1P2 scheme is one of its most attractive features. Dumbser et al. [35] have come to the same conclusion for scalar advection with PNPM schemes and our finding for the induction equation supplements, and yet extends, that finding.

Table II Accuracy analysis (Plane Wave test) of P=1 DG scheme with SSP-RK2 timestepping and CFL = 0.300295. The total magnetic energy on the mesh as a fraction of the initial magnetic energy is also shown.

	L_1 Error	L_1 Accuracy	L_∞ Error	L_∞ Accuracy	Total Magnetic Energy
8×8	9.972E-01		2.169E+00		0.758328061
16×16	1.721E-01	2.535	4.027E-01	2.429	0.962654963
32×32	3.310E-02	2.378	7.641E-02	2.398	0.995110883
64×64	7.372E-03	2.167	1.913E-02	1.998	0.999382357
128×128	1.760E-03	2.067	5.293E-03	1.854	0.999922570
256×256	4.321E-04	2.026	1.387E-03	1.932	0.999990312

512×512	1.072E-04	2.011	3.546E-04	1.967	0.999998789

Table III Accuracy analysis (Plane Wave test) of P=2 DG scheme with SSP-RK3 timestepping and CFL = 0.196555. The total magnetic energy on the mesh as a fraction of the initial magnetic energy is also shown.

	L_1 Error	L_1 Accuracy	L_∞ Error	L_∞ Accuracy	Total Magnetic Energy
8×8	7.609E-01		1.503E+00		0.798233687
16×16	1.062E-01	2.841	2.098E-01	2.841	0.969491429
32×32	1.355E-02	2.970	2.684E-02	2.966	0.996044391
64×64	1.698E-03	2.997	3.369E-03	2.994	0.999501860
128×128	2.123E-04	3.000	4.213E-04	2.999	0.999937630
256×256	2.652E-05	3.001	5.265E-05	3.000	0.999992201
512×512	3.315E-06	3.000	6.582E-06	3.000	0.999999025

Table IV Accuracy analysis (Plane Wave test) of P0P2 scheme with SSP-RK3 timestepping and CFL = 0.671745. The total magnetic energy on the mesh as a fraction of the initial magnetic energy is also shown.

	L_1 Error	L_1 Accuracy	L_∞ Error	L_∞ Accuracy	Total Magnetic Energy
8×8	1.642E+00		3.305E+00		0.592387535
16×16	2.362E-01	2.797	4.628E-01	2.836	0.933337820
32×32	2.966E-02	2.993	5.781E-02	3.001	0.991374277
64×64	3.690E-03	3.007	7.127E-03	3.020	0.998917626
128×128	4.599E-04	3.004	8.832E-04	3.013	0.999864685
256×256	5.741E-05	3.002	1.099E-04	3.006	0.999983082

512×512	7.172E-06	3.001	1.371E-05	3.003	0.999997885

Table V Accuracy analysis (Plane Wave test) of P1P2 scheme with SSP-RK3 timestepping and CFL = 0.300295. The total magnetic energy on the mesh as a fraction of the initial magnetic energy is also shown.

	L_1 Error	L_1 Accuracy	L_∞ Error	L_∞ Accuracy	Total Magnetic Energy
8×8	7.504E-01		1.586E+00		0.796984212
16×16	1.073E-01	2.806	2.181E-01	2.862	0.969180584
32×32	1.383E-02	2.955	2.783E-02	2.970	0.995979229
64×64	1.741E-03	2.990	3.469E-03	3.004	0.999492593
128×128	2.179E-04	2.998	4.314E-04	3.008	0.999936436
256×256	2.725E-05	3.000	5.373E-05	3.005	0.999992050
512×512	3.406E-06	3.000	6.703E-06	3.003	0.999999006

VII.2) Magnetized Vortex Test Problem

We wish to showcase the capabilities of the divergence-free scheme for the induction equation without using any limiters. Unfortunately, most MHD problems will have strong non-linearities which will cause the limiter to be invoked at least some times. We, therefore, pick a test problem which retains the linearity of the induction equation while being as close as possible to a real MHD test problem. The problem we choose consists of using just the magnetic field part of the magnetized vortex test problem that was discussed in Section VI of Balsara [6]. The magnetic field in that problem is extremely smooth and it does not invoke limiters.

The problem is set up on a periodic two-dimensional domain given by [-5,5]X[-5,5]. The velocity of the flow is taken to be $\left(\mathrm{v}_x, \mathrm{v}_y\right) = (1,1)$. Since we only solve the induction equation, there are no density and pressure variables in this test problem. The vortex is initialized at the center of the computational domain with a magnetic field given by

$$\left(B_x , B_y \right) = e^{0.5\left(1-r^2\right)} \left(-y, x \right)$$

The corresponding magnetic vector potential is given by

$$A_z = e^{0.5\left(1-r^2\right)}$$

The problem is run to a time of 10 units, by which point the vortex has propagated along the diagonal of the computational domain and come back to its original location. The errors in the L_1 and L_∞ norms are measured at this final time. We also document the amount of magnetic energy that is retained on the mesh at this final time. It is a good measure of the scheme's ability to preserve magnetic energy.

It is beneficial to show the results in tabulated form as well as in figures. Table VI shows the results for the magnetic vortex test problem for a P=1 DG scheme. We see that it meets its design accuracy. Realize however, that much of the variation in the magnetic field is restricted to a unit radius, which corresponds to one-fifth of the computational domain. We see that for this test problem, we have to go to rather large meshes, with 64×64 zones, before 95% or more of the magnetic energy is preserved. Table VII shows the results for the magnetic vortex test problem for a P=2 DG scheme. While it meets its design accuracy, we can also see that it preserves 95% or more of the magnetic energy on a mesh with 32×32 zones. Now consider the results from Table VIII which pertains to a P0P2 scheme; i.e. this is just a second order WENO scheme. While it also meets its design accuracy, the WENO scheme only preserves 95% or more of its original magnetic energy on a 64×64 mesh. Now consider the P1P2 scheme shown in Table IX. The P1P2 scheme can be run with a CFL which is much larger than the P=2 DG scheme. Even so, its accuracy is entirely comparable to that of the P=2 DG scheme. Furthermore, it can preserve 95% or more of the magnetic energy on a 32×32 zone mesh, just like the P=2 DG scheme.

Fig. 8 shows all the data from Tables VI to IX in a single set of plots. Figs. 8a and 8b show the L_1 and L_∞ errors as a function of mesh size measured along one of the edges of the mesh. We see that there is a quality gap between the P0P1 scheme and the P1P1 scheme (which is indeed the P=1 DG scheme). Likewise, we see a quality gap between the P0P2 scheme (WENO scheme) and the P2P2 scheme (which is indeed the P=2 DG scheme). However, the

P1P2 and P2P2 schemes produce results in Figs. 8a and 8b are virtually indistinguishable! Fig. 8c shows the magnetic energy that is preserved on the mesh at the final time in the simulation as a function of mesh size. Again, we see that the P1P2 and P2P2 schemes' results in Figs. 8c are virtually indistinguishable. This gives us a very good insight, and the very useful suggestion, that PNPM schemes with low (but non-zero) values of "N" might be useful schemes in constraint-preserving computational electrodynamics and computational MHD.

Table VI Accuracy analysis (Magnetic Vortex test) of P=1 DG scheme with SSP-RK2 timestepping and CFL = 0.300295. The total magnetic energy on the mesh as a fraction of the initial magnetic energy is also shown.

	L_1 Error	L_1 Accuracy	L_∞ Error	L_∞ Accuracy	Total Magnetic Energy
8×8	1.136E+01		1.558E+00		0.315708777
16×16	4.349E+00	1.386	7.604E-01	1.035	0.315708777
32×32	8.884E-01	2.292	2.123E-01	1.841	0.315708777
64×64	1.498E-01	2.568	3.977E-02	2.416	0.991039970
128×128	2.934E-02	2.353	7.454E-03	2.416	0.991039970
256×256	6.704E-03	2.130	7.454E-03	2.273	0.991039970
512×512	1.639E-03	2.033	3.489E-04	2.144	0.999981950

Table VII Accuracy analysis (Magnetic Vortex test) of P=2 DG scheme with SSP-RK3 timestepping and CFL = 0.196555. The total magnetic energy on the mesh as a fraction of the initial magnetic energy is also shown.

	L_1 Error	L_1 Accuracy	L_∞ Error	L_∞ Accuracy	Total Magnetic Energy
8×8	9.938E+00		1.162E+00		0.519655482

16×16	3.292E+00	1.594	4.590E-01	1.339	0.822776045
32×32	5.865E-01	2.489	9.850E-02	2.220	0.965903039
64×64	7.968E-02	2.880	1.446E-02	2.768	0.995301999
128×128	1.013E-02	2.976	1.864E-03	2.956	0.999402788
256×256	1.276E-03	2.989	2.342E-04	2.992	0.999925126
512×512	1.629E-04	2.969	6.350E-05	1.883	0.999990635

Table VIII Accuracy analysis (Magnetic Vortex test) of P0P2 scheme with SSP-RK3 timestepping and CFL = 0.671745. The total magnetic energy on the mesh as a fraction of the initial magnetic energy is also shown.

	L_1 Error	L_1 Accuracy	L_∞ Error	L_∞ Accuracy	Total Magnetic Energy
8×8	1.320E+01		1.930E+00		0.041739861
16×16	7.906E+00	0.739	1.334E+00	0.533	0.258680606
32×32	1.915E+00	2.045	3.944E-01	1.758	0.820789577
64×64	3.232E-01	2.567	7.097E-02	2.474	0.973056493
128×128	4.182E-02	2.950	9.481E-03	2.904	0.996513907
256×256	5.256E-03	2.992	1.196E-03	2.987	0.999562555
512×512	6.695E-04	2.973	1.495E-04	3.000	0.999945297

Table IX Accuracy analysis (Magnetic Vortex test) of P1P2 scheme with SSP-RK3 timestepping and CFL = 0.300295. The total magnetic energy on the mesh as a fraction of the initial magnetic energy is also shown.

	L_1 Error	L_1 Accuracy	L_∞ Error	L_∞ Accuracy	Total Magnetic Energy
8×8	1.018E+01		1.390E+00		0.363160943

16×16	3.339E+00	1.609	5.206E-01	1.417	0.776986515
32×32	5.893E-01	2.502	9.866E-02	2.400	0.963500507
64×64	8.002E-02	2.881	1.392E-02	2.825	0.995203432
128×128	1.022E-02	2.970	1.876E-03	2.891	0.999393772
256×256	1.293E-03	2.983	2.368E-04	2.986	0.999924043
512×512	1.675E-04	2.948	6.830E-05	1.794	0.999990499

VIII) Conclusions

The induction equation plays an important role in MHD and other systems of equations like it. Numerical MHD, which requires the constrained evolution of the magnetic field, is a very prominent example of such a mimetic scheme. We see that it is important to evolve the magnetic field in the induction equation in a globally divergence-free fashion. This is best done on a staggered Yee-type mesh. On such a mesh, the magnetic field components are collocated at the faces of the mesh while the electric field components reside at the edges of the mesh. Finite volume schemes have already been extended to accommodate such a collocation of variables (Balsara and Spicer [4], Balsara [6], [7], Balsara and Dumbser [20], Xu *et al*. [49]). The present work extends RKDG schemes to accomodate the induction equation. This is done with the help of two important algorithmic advances.

In our first algorithmic advance, we build on prior work on divergence-free reconstruction of vector fields (Balsara [5], [6], [7], Balsara and Dumbser [20], Xu *et al*. [49]) to extend DG formulations so that they can accommodate a globally divergence-free reconstruction process. Consequently, at the faces of each mesh, we store the magnetic field components as well as its higher moments. A DG formulation is then developed that operates on the faces of the mesh. The DG update requires the electric fields at the edges of the mesh. For finite volume schemes for MHD, recent advances in multidimensional Riemann solvers (Balsara [13], [14], [17], [19], Balsara, Dumbser & Abgrall [15] and Balsara & Dumbser [17], Vides *et al*. [48], Balsara *et al*. [21], [22]) have made it possible to uniquely define the edge-centered electric field in a multidimensionally upwinded fashion. Our second algorithmic advance consists of integrating multidimensional Riemann solvers with DG schemes for the induction equation. Just as the fluxes from a one-dimensional Riemann solver help in resolving the boundary integrals that arise in a conventional DG scheme, the electric fields from the multidimensional Riemann solvers help in resolving the edge integrals that arise in the DG scheme for the induction equation. While the two-dimensional case is discussed here, the method is, however, very general and also applies to three dimensions or to unstructured meshes.

When the velocity is pre-specified in the induction equation, the DG scheme becomes linear in the magnetic field variables. This simplification is used to carry out a von Neumann stability analysis of DG schemes for the induction equation. We stress that the induction equation is inherently multidimensional, so the stability analysis should also be multidimensional.

Results from the stability analysis are presented showing that the induction equation permits CFL numbers that are comparable to traditional RKDG schemes. We also analyze the wave propagation characteristics of the method and show that with increasing order of accuracy the wave propagation becomes more isotropic and free of dissipation for a larger range of long wavelength modes. This makes a strong case for investing in higher order methods. We also use the von Neumann stability analysis to show that that the divergence-free reconstruction and multidimensional Riemann solvers are essential algorithmic ingredients of a globally divergence-free RKDG scheme.

A numerical accuracy analysis of the RKDG schemes is presented up to third order. We also study the accuracy of comparable PNPM schemes. It is found that the P1P2 scheme offers accuracy that is entirely comparable to the P=2 DG scheme, while permitting a larger CFL number.

Acknowledgements

Both authors gratefully acknowledge Sid Mishra for very helpful discussions. DSB acknowledges support via NSF grants NSF-DMS-1361197, NSF-ACI-1533850 and NSF-DMS-1622457. RK was supported in part by ERC STG. N 306279, SPARCCLE. Several simulations were performed on a cluster at UND that is run by the Center for Research Computing. Computer support on NSF's XSEDE and Blue Waters computing resources is also acknowledged. The authors acknowledge the computational resources provided by the BRUTUS and EULER clusters of ETHZ.

References

[1] D. S. Balsara, *Linearized formulation of the Riemann problem for adiabatic and isothermal magnetohydrodynamics*, Astrophysical Journal Supplement 116 (1998) 119

[2] D.S. Balsara, *Total variation diminishing algorithm for adiabatic and isothermal magnetohydrodynamics*, Astrophysical Journal Supplement 116 (1998) 133

[3] D. S. Balsara and D. S. Spicer, *Maintaining pressure positivity in magnetohydrodynamic simulations*, Journal of Computational Physics 148 (1999) 133-148

[4] D. S. Balsara and D. S. Spicer, *A staggered mesh algorithm using high order Godunov fluxes to ensure solenoidal magnetic fields in magnetohydrodynamic simulations*, Journal of Computational Physics 149 (1999) 270-292

[5] D.S. Balsara ,*Divergence-free adaptive mesh refinement for magnetohydrodynamics*, Journal of Computational Physics 174 (2001) 614-648

[6] D. S. Balsara, *Second-order-accurate schemes for magnetohydrodynamics with divergence-free reconstruction*, Astrophysical Journal Supplement 151 (2004) 149-184

[7] D.S. Balsara, *Divergence-free reconstruction of magnetic fields and WENO schemes for magnetohydrodynamics*, J. Comput. Phys., 228 (2009) 5040-5056

[8] D.S. Balsara& J.S. Kim, *An Intercomparison Between Divergence-Cleaning and Staggered Mesh Formulations for Numerical Magnetohydrodynamics*, Astrophysical Journal 602 (2004) 1079

[9] D. S. Balsara and C.-W. Shu, *Monotonicity Preserving Weighted Non-oscillatory schemes with increasingly High Order of Accuracy*, Journal of Computational Physics 160 (2000) 405-452

[10] D. S. Balsara, C. Altmann, C.D. Munz, M. Dumbser, *A sub-cell based indicator for troubled zones in RKDG schemes and a novel class oh hybrid RKDG+HWENO schemes*, Journal of Computational Physics 226 (2007) 586- 620

[11] D.S. Balsara, T. Rumpf, M. Dumbser and C.-D.Munz, *Efficient, high accuracyADER-WENO schemes for hydrodynamics and divergence-free magnetohydrodynamics*, Journal of Computational Physics 228 (2009) 2480-2516

[12] Balsara, D.S., Dumbser, M., Meyer, C., Du, H. & Xu, Z., *Efficient Implementation of ADER schemes for Euler and Magnetohydrodynamic flow on structured meshes – Comparison with Runge-Kutta methods*, Journal of Computational Physics, 235 (2013) 934-969

[13] D.S. Balsara, *Multidimensional HLLE Riemann solver; Application to Euler and Magnetohydrodynamic Flows*, J. Comput. Phys., 229 (2010) 1970-1993

[14] D.S. Balsara, *A two-dimensional HLLC Riemann solver for conservation laws: Application to Euler and magnetohydrodynamic flows*, Journal of Computational Physics 231 (2012) 7476-7503

[15] D.S. Balsara, M. Dumbser and R. Abgrall, *Multidimensional HLL and HLLC Riemann Solvers for Unstructured Meshes – With Application to Euler and MHD Flows*, Journal of Computational Physics 261 (2014) 172-208

[16] D.S. Balsara, *Multidimensional Riemann Problem with Self-Similar Internal Structure – Part I – Application to Hyperbolic Conservation Laws on Structured Meshes*, to appear, Journal of Computational Physics (2014)

[17] D.S. Balsara and M. Dumbser, *Multidimensional Riemann Problem with Self-Similar Internal Structure – Part II – Application to Hyperbolic Conservation Laws on Unstructured Meshes*, submitted, Journal of Computational Physics (2014)

[18] Balsara, D.S., *Self-Adjusting, Positivity Preserving High Order Schemes for Hydrodynamics and Magnetohydrodynamics*, Journal of Computational Physics, 231 (2012) 7504-7517

[19] D.S. Balsara, *Three Dimensional HLL Riemann Solver for Structured Meshes; Application to Euler and MHD Flow*, Journal of Computational Physics 295 (2015) 1-23

[20] Balsara, D.S. and Dumbser, M., Divergence-Free MHD on Unstructured Meshes Using High Order Finite Volume Schemes Based on Multidimensional Riemann Solvers, to appear Journal of Computational Physics, (2015)

[21] D.S. Balsara, J. Vides, K. Gurski, B. Nkonga, M. Dumbser, S. Garain, E. Audit, *A Two-Dimensional Riemann Solver with Self-Similar Sub-Structure – Alternative Formulation Based on Least Squares Projection*, Journal of Computational Physics, 304 (2016a) 138-161

[22] D.S. Balsara , B. Nkonga, M. Dumbser and C.-D. Munz, *Formulating Multidimensional Riemann Solvers in Similarity Variables – Part III :A Multidimensional Analogue of the HLLEM Riemann Solver for Conservative Hyperbolic Systems*, in preparation, Journal of Computational Physics (2016c)

[23] J. U. Brackbill and D. C. Barnes, *The effect of nonzero* $\nabla \cdot \boldsymbol{B}$ *on the numerical solution of the magnetohydrodynamic equations*, Journal of Computational Physics 35 (1980) 426-430

[24] J. Brackbill, *Fluid modelling of magnetized plasmas*, Space Sci. Rev. 42 (1985) 153

[25] Y. Cheng, F. Li, J. Qiu & L. Xu, *Positivity-preserving DG and central DG methods for ideal MHD equations*, J. Comput. Phys., 238 (2013) 255

[26] A.J. Christlieb, J.A. Rossmanith and Q. Tang, *Finite difference weighted essentially non-oscillatory schemes with constrained transport for ideal magnetohydrodynamics*, J. Comput. Phys., 268 (2014) 302-325

[27] Cockburn, B. and Shu, C.-W., *TVB Runge-Kutta local projection discontinuous Galerkin finite element method for conservation laws II: general framework*, Mathematics of Computation, 52 (1989) 411-435

[28] Cockburn, B., Hou, S., and Shu, C.-W., *TVB Runge-Kutta local projection discontinuous Galerkin finite element method for conservation laws IV: The multidimensional case*, Journal of Computational Physics, 54 (1990) 545-581

[29] Cockburn, B., and Shu, C.-W., *The Runge-Kutta discontinuous Galerkin method for Conservation Laws V : Multidimensional systems*, Journal of Computational Physics, 141 (1998) 199-224

[30] Cockburn, B., Karniadakis, G., and Shu, C.-W., *The development of discontinuous Galerkin Methods, in Discontinuous Galerkin Methods: Theory, Computation and Applications*, B. Cockburn, G. Karniadakis and C.-W. Shu, editors, Lecture Notes in Computational Science and Engineering, volume 11, Springer, 2000, Part I: Overview, 3-50.

[31] Cockburn, B., and Shu, C.-W., *Runge-Kutta Discontinuous Galerkin methods for convection dominated problems*, Journal of Scientific computing 16 (2001) 173-261

[32] B. Cockburn F. Li and C.-W. Shu, *Locally divergence-free discontinuousGalerkin method for the Maxwell equations*, Journal of Computational Physics 141 (2005) 413-442

[33] P. Colella, *Multidimensional upwind methods for conservation laws*, Journal of Computational Physics 87 (1990) 171

[36] W. Dai and P.R. Woodward, *On the divergence-free condition and conservationlaws in numerical simulations for supersonic magnetohydrodynamic flows*, Astrophysical Journal 494 (1998) 317-335

[35] M. Dumbser, D. Balsara, E.F. Toro, C.D. Munz, *A unified framework for the construction of one-step finite volume and discontinuous Galerkin schemes on unstructured meshes*, Journal of Computational Physics 227 (2008) 8209-8253

[36] M. Dumbser, O. Zanotti, A. Hidalgo and D.S. Balsara, *ADER-WENO Finite Volume Schemes with Space-Time Adaptive Mesh Refinement*, J. Comp. Phys. Vol. 248, Pgs. 257-286 (2013)

[37] T. Gardiner & J.M. Stone, *An unsplit Godunov method for ideal MHD via constrained transport*, Journal of Computational Physics, 205 (2005), 509

[38] S. Gottlieb, *On higher order strong stability preserving Runge-Kutta and multistep time discretizations*, Journal of Scientific Computing, 25 (1/2) (2005) 105

[39] S. Gottlieb, C.-W. Shu, E. Tadmor, *Strong stability-preserving higher order time discretization methods*, SIAM Review, 43(1) (2001) 89-112

[40] F. Li, L. Xu and S. Yakovlev,*Central discontinuous Galerkin methods for ideal MHD equations with the exactly divergence-free magnetic field*, J. Comput. Phys., 230(12) (2011) 4828-4847

[41] Y. Liu, C.-W. Shu, E. Tadmor and M. Zhang, *L2 stability analysis of the central discontinuous Galerkin method and comparison between the central and regular discontinuous Galerkin methods*, Math. Model. Numer. Anal., 42 (2008) 593-607

[42] P. Londrillo and L. DelZanna, *On the divergence-free condition in Godunov-type schemes for ideal magnetohydrodynamics: the upwind constrained transport method*, Journal of Computational Physics 195 (2004) 17-48

[43] W. H. Reed and T. R. Hill, *Triangular mesh methods for the neutron transport equation*, Tech. Report LA-UR-73-479, Los Alamos Scientific Laboratory, (1973).

[44] D. Ryu, F. Miniati, T. W. Jones, and A. Frank, *A divergence-free upwind code for multidimensional magnetohydrodynamic flows*, Astrophysical Journal 509 (1998) 244-255

[45] Shu, C.-W., *Total variation-diminishing time discretizations*, SIAM Journal of Scientific and Statistical Computing, 9 (1988) 1073-1084

[46] Spiteri, R.J. and Ruuth, S.J., *A new class of optimal high-order strong-stability-preserving time-stepping schemes*, SIAM Journal of Numerical Analysis, 40 (2002), pp. 469–491

[47] A.Taube, M. Dumbser, D.S, Balsara & C.D. Munz, Arbitrary High Order Discontinuous Galerkin Schemes for the MHD Equations, SIAM J. Scientific Computing, Vol. 30(3) (2007) 441-461

[48] J. Vides, B. Nkonga and E. Audit, *A simple two-dimensional extension of the HLL Riemann solver for hyperbolic conservation laws*, J. Comput. Phys., 280(1) (2015) 643-675

[49] Z. Xu, D. S. Balsara & H. Du, *Divergence-free WENO Reconstruction-based finite volume scheme for solving ideal MHD equations on triangular meshes,* submitted, Communications in Computational Physics (2015)

[50] H. Yang and F. Li, *Stability analysis and error estimates of an exactly divergence-free method for the magnetic induction equations*, ESAIM: Mathematical Modelling and Numerical Analysis, 50(4) (2016) 965-993

[51] K.S. Yee, *Numerical Solution of Initial Boundary Value Problems Involving Maxwell Equation in an Isotropic Media*, IEEE Trans. Antenna Propagation 14 (1966) 302

[52] A.H. Stroud, *Approximate Calculation of Multiple Integrals*, Prentice-Hall Inc., Englewood Cliffs, NJ, 1971.

[52] M. Zhang and C.-W. Shu, *An analysis of and a comparison between the discontinuous Galerkin and the spectral finite volume methods*, Computers and Fluids, 34 (2005) 581-592

Appendix A

We request the reader to focus on Fig. 1a. At second order, matching the linearly varying part of the x-component of the magnetic field in the right and left x-faces gives

$$a_y = \left(B_y^{x+} + B_y^{x-}\right)/2 \quad ; \quad a_{xy} = B_y^{x+} - B_y^{x-} \quad ; \quad b_{yy} = -a_{xy}/2 \tag{A.1}$$

Matching the linearly varying part of the y-component of the magnetic field in the top and bottom y-faces gives

$$b_x = \left(B_x^{y+} + B_x^{y-}\right)/2 \quad ; \quad b_{xy} = B_x^{y+} - B_x^{y-} \quad ; \quad a_{xx} = -b_{xy}/2 \tag{A.2}$$

Matching the constant part of the x-component of the magnetic field in the right and left x-faces gives

$$a_0 = \left(B_0^{x+} + B_0^{x-}\right)/2 - a_{xx}/6 \quad ; \quad a_x = B_0^{x+} - B_0^{x-} \tag{A.3}$$

Matching the constant part of the y-component of the magnetic field in the top and bottom y-faces gives

$$b_0 = \left(B_0^{y+} + B_0^{y-}\right)/2 - b_{yy}/6 \quad ; \quad b_y = B_0^{y+} - B_0^{y-} \tag{A.4}$$

It is easy to show that the constraint $a_x + b_y = 0$ refers to the divergence-free aspect of the magnetic field. This completes our description of the divergence-free reconstruction of magnetic fields at second order.

Appendix B

Let the mean x-components of the magnetic field in the right and left faces of the reference square be denoted by $B_0^{x\pm}$ respectively; let the corresponding first moments within those faces be denoted by $B_y^{x\pm}$ respectively; let the corresponding second moments in those faces be denoted by $B_{yy}^{x\pm}$ respectively. The two piecewise parabolic profiles for the x-component of the magnetic field at the right and left faces of the reference element are given by

$$B^{x\pm}\left(y\right)=B_0^{x\pm}+B_y^{x\pm}y+B_{yy}^{x\pm}\left(y^2-1/12\right) \tag{B.1}$$

Similarly, let the mean y-components of the magnetic field in the top and bottom faces of the reference square be denoted by $B_0^{y\pm}$ respectively; let the corresponding first moments within those faces be denoted by $B_x^{y\pm}$ respectively; let the corresponding second moments in those faces be denoted by $B_{xx}^{y\pm}$ respectively. The two piecewise parabolic profiles for the y-component of the magnetic field at the top and bottom faces of the reference element are given by

$$B^{y\pm}\left(x\right)=B_0^{y\pm}+B_x^{y\pm}x+B_{xx}^{y\pm}\left(x^2-1/12\right) \tag{B.2}$$

The reconstructing polynomials for the magnetic field within the reference element are given by

$$\begin{aligned} B^x(x,y) &= a_0 + a_x\,x + a_y\,y + a_{xx}\left(x^2-1/12\right) + a_{xy}\,x\,y + a_{yy}\left(y^2-1/12\right) \\ &\quad + a_{xxx}\left(x^3-3x/20\right) + a_{xyy}\,x\left(y^2-1/12\right) \\ B^y(x,y) &= b_0 + b_x\,x + b_y\,y + b_{xx}\left(x^2-1/12\right) + b_{xy}\,x\,y + b_{yy}\left(y^2-1/12\right) \\ &\quad + b_{xxy}\left(x^2-1/12\right)y + b_{yyy}\left(y^3-3y/20\right) \end{aligned} \tag{B.3}$$

Applying the divergence-free constraint at all points within the reference element gives

$$\begin{gathered} 3\,a_{xxx}+b_{xxy}=0 \;;\quad a_{xyy}+3\,b_{yyy}=0 \;;\quad 2\,a_{xx}+b_{xy}=0 \;;\quad a_{xy}+2\,b_{yy}=0 \;; \\ a_x+b_y-\left(a_{xyy}+b_{xxy}\right)\big/30=0 \end{gathered} \tag{B.4}$$

Eqns. (B.3) and (B.4) specify eleven independent coefficients in the interior of the reference square which should be used to match the eleven independent pieces of information specified at the boundaries of the reference square via eqns. (B.1) and (B.2)

Matching the second moments gives

$$\begin{aligned} &a_{yy} = \left(B_{yy}^{x+} + B_{yy}^{x-}\right)\big/2 \quad ; \quad a_{xyy} = B_{yy}^{x+} - B_{yy}^{x-} \quad ; \quad b_{xx} = \left(B_{xx}^{y+} + B_{xx}^{y-}\right)\big/2 \quad ; \quad b_{xxy} = B_{xx}^{y+} - B_{xx}^{y-} \quad ; \\ &a_{xxx} = -b_{xxy}/3 \quad ; \quad b_{yyy} = -a_{xyy}/3 \end{aligned} \tag{B.5}$$

Matching the first moments gives

$$\begin{aligned} &a_{y} = \left(B_{y}^{x+} + B_{y}^{x-}\right)\big/2 \quad ; \quad a_{xy} = B_{y}^{x+} - B_{y}^{x-} \quad ; \quad b_{x} = \left(B_{x}^{y+} + B_{x}^{y-}\right)\big/2 \quad ; \quad b_{xy} = B_{x}^{y+} - B_{x}^{y-} \quad ; \\ &a_{xx} = -b_{xy}\big/2 \quad ; \quad b_{yy} = -a_{xy}\big/2 \end{aligned} \tag{B.6}$$

Matching the zeroth moments gives

$$\begin{aligned} &a_{0} = \left(B_{0}^{x+} + B_{0}^{x-}\right)\big/2 - a_{xx}\big/6 \quad ; \quad a_{x} = \left(B_{0}^{x+} - B_{0}^{x-}\right) + b_{xxy}\big/30 \quad ; \\ &b_{0} = \left(B_{0}^{y+} + B_{0}^{y-}\right)\big/2 - b_{yy}\big/6 \quad ; \quad b_{y} = \left(B_{0}^{y+} - B_{0}^{y-}\right) + a_{xyy}\big/30 \end{aligned} \tag{B.7}$$

Eqns. (B.5), (B.6) and (B.7) should be implemented in computer code in the same sequence that we have used to document them here. It is easy to see that

$$a_{x} + b_{y} - \left(a_{xyy} + b_{xxy}\right)\big/30 = \left(B_{0}^{x+} - B_{0}^{x-}\right) + \left(B_{0}^{y+} - B_{0}^{y-}\right) \tag{B.8}$$

Since the right hand side of the above equation is just the divergence-free condition applied to the reference square, it is easy to see that it should be zero. Thus, all the constraints in eqn. (B.4) are satisfied by our third order accurate divergence-free reconstruction.

Appendix C

For the multidimensional HLL Riemann solver, it is possible to do something that closely mimics the propagation of fast magnetosonic waves in MHD. We assume that we are dealing with the sub-sonic case. Since fast magnetosonic waves (unlike hydrodynamical sound waves) can travel at different speeds in the x- and y-directions, we assume that the x-directional wave propagation is bounded by $\left[\mathrm{v}_x - c_x, \mathrm{v}_x + c_x\right]$ where c_x is some proxy for a fast magnetosonic speed in the x-direction. Because the flow is assumed sub-sonic, we have $c_x > \left|\mathrm{v}_x\right|$. Likewise, the y-directional wave propagation is bounded by $\left[\mathrm{v}_y - c_y, \mathrm{v}_y + c_y\right]$ where c_y is some proxy for the fast magnetosonic speed in the y-direction. Again, because the flow is assumed sub-sonic, we have $c_y > \left|\mathrm{v}_y\right|$. We cannot specify c_x and c_y any further for the induction equation because there isn't enough physics in the induction equation to motivate a concept of a fast magnetosonic speed. But we can always assume that the induction equation is part of some larger system that admits a fast magnetosonic speed. For numerical examples in this paper, we will always take $c_x = 1.2\ |\mathrm{v}_x|$ and $c_y = 1.2\ |\mathrm{v}_y|$, which ensures that our one-dimensional Riemann problems are subsonic. As a result, the multidimensional HLL Riemann solver is also sub-sonic. The multidimensional wave model of the multidimensional HLL Riemann solver is given by $\left[\mathrm{v}_x - c_x, \mathrm{v}_x + c_x\right] \times \left[\mathrm{v}_y - c_y, \mathrm{v}_y + c_y\right]$. Once the wave model and the incoming states are specified, the electric field from the multidimensional HLL Riemann solver can be computed using eqns. (12), (13) and (14) of Balsara [16]. It is given by

$$\begin{aligned} E^z_{HLL} &= \mathrm{v}_y \left(B^x_{RU} + B^x_{LU} + B^x_{LD} + B^x_{RD} \right) \big/ 4 - \mathrm{v}_x \left(B^y_{RU} + B^y_{LU} + B^y_{LD} + B^y_{RD} \right) \big/ 4 \\ &\quad - \frac{c_y}{4} \left(\left(B^x_{RU} + B^x_{LU} \right) \big/ 2 - \left(B^x_{RD} + B^x_{LD} \right) \big/ 2 \right) + \frac{c_x}{4} \left(\left(B^y_{RU} + B^y_{RD} \right) \big/ 2 - \left(B^y_{LU} + B^y_{LD} \right) \big/ 2 \right) \end{aligned} \tag{C.1}$$

Like eqn. (4.1), the first line of the above equation yields the centered electric field. The second line in the above equation contains the dissipation terms. We see that the dissipation terms from the multidimensional HLL Riemann solver can be as small as half the dissipation terms from the multidimensional LF Riemann solver. (In all fairness, the dissipation also depends on the magnitude of c_x and c_y.) This is an expected trend and is also reflected in any cross-comparison of the one-dimensional HLL and LF Riemann solvers.

Appendix D

Here we provide explicit forms for the coefficients in eqn. (5.11) which pertain to the P=1 DG scheme. They are:

$$A_{11} = \frac{1}{2\ \Delta x\ \Delta y} \begin{bmatrix} \sqrt{3}\ \Delta y\ \mathrm{v}_x \left(\cos\left(k_x \Delta x\right) - 1 \right) + \left(\Delta x + \Delta y \right) \left| \mathrm{v}_x \right| \cos\left(k_x \Delta x\right) - 2\ \Delta x\ \left| \mathrm{v}_y \right| \left(\cos\left(k_y \Delta y\right) + 2 \right) \\ -i\ \left(\Delta x + \Delta y \right)\ \mathrm{v}_x \sin\left(k_x \Delta x\right) - \left| \mathrm{v}_x \right| \left(\Delta x + \Delta y + i\ \sqrt{3}\ \Delta y \sin\left(k_x \Delta x\right) \right) + 2\ i\ \Delta x\ \mathrm{v}_y \sin\left(k_y \Delta y\right) \end{bmatrix}$$

$$A_{12}=\frac{1}{2\ \Delta x\ \Delta y}\left[\begin{array}{l}\sqrt{3}\ \left(-\Delta y\ \mathrm{v}_x-2\ \Delta x\ \mathrm{v}_y+\Delta y\ \mathrm{v}_x\cos\left(k_x\Delta x\right)\right)+i\ \left(\Delta x-\Delta y\right)\ \mathrm{v}_x\sin\left(k_x\Delta x\right)\\ +\left|\mathrm{v}_x\right|\left(\Delta x-\Delta y+\left(-\Delta x+\Delta y\right)\cos\left(k_x\Delta x\right)-i\ \sqrt{3}\ \Delta y\ \sin\left(k_x\Delta x\right)\right)\\ +2\ \Delta x\left(\left|\mathrm{v}_y\right|+\left(\sqrt{3}\ \mathrm{v}_y+2\ \left|\mathrm{v}_y\right|\right)\cos\left(k_y\Delta y\right)-i\ \left(2\ \mathrm{v}_y+\sqrt{3}\left|\mathrm{v}_y\right|\right)\sin\left(k_y\Delta y\right)\right)\end{array}\right]$$

$$A_{13}=\frac{-\sqrt{3}\left(1-e^{-ik_y\Delta y}\right)}{2\ \Delta y}\left[\mathrm{v}_x+\left|\mathrm{v}_x\right|+e^{ik_x\Delta x}\left(\left|\mathrm{v}_x\right|-\mathrm{v}_x\right)\right]$$

$$A_{21}=\frac{1}{2\ \Delta x\ \Delta y}\left[\begin{array}{l}\sqrt{3}\ \left(-\Delta y\ \mathrm{v}_x+2\ \Delta x\ \mathrm{v}_y+\Delta y\ \mathrm{v}_x\cos\left(k_x\Delta x\right)\right)+i\ \left(\Delta x-\Delta y\right)\ \mathrm{v}_x\sin\left(k_x\Delta x\right)\\ +\left|\mathrm{v}_x\right|\left(\Delta x-\Delta y+\left(-\Delta x+\Delta y\right)\cos\left(k_x\Delta x\right)-i\ \sqrt{3}\ \Delta y\ \sin\left(k_x\Delta x\right)\right)\\ -2\ \Delta x\ \mathrm{v}_y\left(\sqrt{3}\cos\left(k_y\Delta y\right)+2\ i\ \sin\left(k_y\Delta y\right)\right)+2\ \Delta x\ \left|\mathrm{v}_y\right|\left(1+2\cos\left(k_y\Delta y\right)+i\ \sqrt{3}\ \sin\left(k_y\Delta y\right)\right)\end{array}\right]$$

$$A_{22}=A_{11}$$

$$A_{23}=A_{13}$$

$$A_{31}=\left[\begin{array}{l}-\Delta x\left|\mathrm{v}_y\right|+\left(\Delta x-\Delta y\right)\left|\mathrm{v}_y\right|\cos\left(k_y\Delta y\right)+\sqrt{3}\left(-2\ \Delta y\ \mathrm{v}_x+\Delta x\ \mathrm{v}_y-\Delta x\ \mathrm{v}_y\cos\left(k_y\Delta y\right)\right)\\ +\Delta y\left(\left|\mathrm{v}_y\right|+2\sqrt{3}\ \mathrm{v}_x\cos\left(k_x\Delta x\right)-4\ i\ \mathrm{v}_x\sin\left(k_x\Delta x\right)+\left|\mathrm{v}_x\right|\left(2+4\cos\left(k_x\Delta x\right)-2\ i\ \sqrt{3}\sin\left(k_x\Delta x\right)\right)\right)\\ -i\ \left(\left(\Delta x-\Delta y\right)\ \mathrm{v}_y-\sqrt{3}\ \Delta x\left|\mathrm{v}_y\right|\right)\sin\left(k_y\Delta y\right)\end{array}\right]$$
$$\times\frac{\left[-i\ \sin\left(k_x\Delta x/2\right)\right]}{\left[\Delta x^2\ e^{i\left(k_x\Delta x/2-k_y\Delta y\right)}\left(e^{ik_y\Delta y}-1\right)\right]}$$

$$A_{32} = \left[\begin{array}{l} -\Delta x \left| \mathrm{v}_y \right| + \left(\Delta x - \Delta y \right) \left| \mathrm{v}_y \right| \cos\left(k_y \Delta y \right) + \sqrt{3} \left(-2 \; \Delta y \; \mathrm{v}_x - \Delta x \; \mathrm{v}_y + \Delta x \; \mathrm{v}_y \cos\left(k_y \Delta y \right) \right) \\ +\Delta y \left(\left| \mathrm{v}_y \right| + 2\sqrt{3} \; \mathrm{v}_x \cos\left(k_x \Delta x \right) - 4 \; i \; \mathrm{v}_x \sin\left(k_x \Delta x \right) + \left| \mathrm{v}_x \right| \left(2 + 4 \cos\left(k_x \Delta x \right) - 2 \; i \; \sqrt{3} \sin\left(k_x \Delta x \right) \right) \right) \\ -i \; \left(\left(\Delta x - \Delta y \right) \; \mathrm{v}_y + \sqrt{3} \; \Delta x \; \left| \mathrm{v}_y \right| \right) \sin\left(k_y \Delta y \right) \end{array} \right]$$

$$\times \frac{\left[-i \; \sin\left(k_x \Delta x / 2 \right) \right]}{\left[\Delta x^2 \; e^{i\left(k_x \Delta x/2 - k_y \Delta y \right)} \left(e^{i k_y \Delta y} - 1 \right) \right]}$$

$$A_{33} = \frac{1}{\Delta x} \left[\begin{array}{l} \sqrt{3} \; \mathrm{v}_x - \sqrt{3} \; \mathrm{v}_x \cos\left(k_x \Delta x \right) + \left| \mathrm{v}_y \right| \left(\cos\left(k_y \Delta y \right) - 1 \right) + 3 \; i \; \mathrm{v}_x \sin\left(k_x \Delta x \right) \\ + \left| \mathrm{v}_x \right| \left(-3 \; - \; 3 \cos\left(k_x \Delta x \right) + i \; \sqrt{3} \; \sin\left(k_x \Delta x \right) \right) - i \; \mathrm{v}_y \sin\left(k_y \Delta y \right) \end{array} \right]$$

Please note that $i \equiv \sqrt{-1}$ in the above equations. Please also note that the square brackets in the previous several equations are not to be confused with matrices. Different choices of quadrature points will result in slightly different expressions and the above terms are specific to choosing two-point Gauss-Legendre quadrature in the faces.

Figure Captions

Fig. 1 shows how the divergence-free reconstruction is carried out in the shaded zone. The profiles of the facial magnetic field components are also shown. Fig. 1a shows piecewise constant magnetic field components in the faces; i.e., the first order case. Fig. 1b shows piecewise linear magnetic field components in the faces; i.e., the second order case.

Fig. 2 shows the four states RU (right-up), LU (left-up), LD (left-down) and RD (right-down) that come together at a vertex. These four states contribute to the multidimensional Riemann problem at that vertex. (Such states are only shown for a few vertices in the figure.) The multidimensional Riemann problem gives us the z-component of the electric field at that vertex. The nodal points that contribute to the update of the central zone for the p=1 RKDG scheme are also shown by dots within each face. Only the filled dots at the nodal points truly contribute to the update of the nodal points that lie on the faces of the (0,0) zone.

Fig 3 shows the domain of stability for the first order (P=0) DG scheme with forward Euler timestepping. The x- and y-axes of the plot show the CFL number in the x- and y-directions. The color shows the amplitude of the amplification factor. The white lines identify the boundary of *the domain of stability. Within the domain of stability, the amplification factor is less than or equal to unity for all possible wave modes that can propagate on the mesh. The CFL number is just the radius of the largest circle (in the Euclidean norm) remaining within the stability region in Fig. 3.*

Fig. 4 shows the domain of stability for the second order (P=1) DG scheme with several different timestepping strategies. Figs. 4a and 4b show the result of using the second and third order SSP schemes from Shu and Osher. Fig. 4c shows the result of using the RK(5,4) scheme from Spiteri and Ruuth. The white curves identify the boundary of the domain of stability. The CFL number is just the radius of the largest circle (in the Euclidean norm) remaining within the stability region in Fig. 4.

Fig. 5 shows the domain of stability for the third order (P=2) DG scheme with several different timestepping strategies. Fig. 5a shows the result of using the third order SSP scheme from Shu and Osher. Fig. 5b shows the result of using the RK(5,4) scheme. The white curves identify the boundary of the domain of stability. The CFL number is just the radius of the largest circle (in the Euclidean norm) remaining within the stability region in Fig. 5.

Figs. 6a, 6b, 6c and 6d show the result of such a wave propagation study when the velocity vector makes angles of 0^o *,* $15\,^o$ *,* $30\,^o$ *and* $45\,^o$ *to the mesh for the second order (P=1) DG scheme with SSP-RK2. Figs. 6 and 7 use the same vertical scale so that the amplification factors at different orders can be cross-compared.*

Figs. 7a, 7b, 7c and 7d are analogous to Fig. 6 but pertain to the third order (P=2) DG scheme with SSP-RK3. We see that the higher order scheme shows better wave propagation in all directions.

Fig. 8 shows all the data from Tables VI to IX in a single set of plots. Figs. 8a and 8b show the L_1 *and* L_∞ *errors as a function of mesh size measured along one of the edges of the mesh. Fig. 8c shows the magnetic energy that is preserved on the mesh at the final time in the simulation as a function of mesh size.*

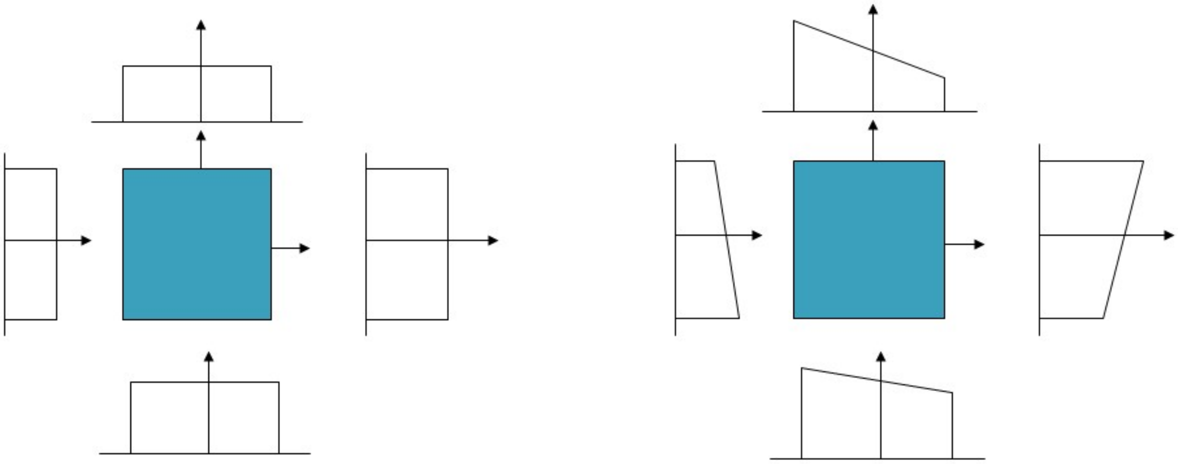

Fig. 1 shows how the divergence-free reconstruction is carried out in the shaded zone. The profiles of the facial magnetic field components are also shown. Fig. 1a shows piecewise constant magnetic field components in the faces; i.e., the first order case. Fig. 1b shows piecewise linear magnetic field components in the faces; i.e., the second order case.

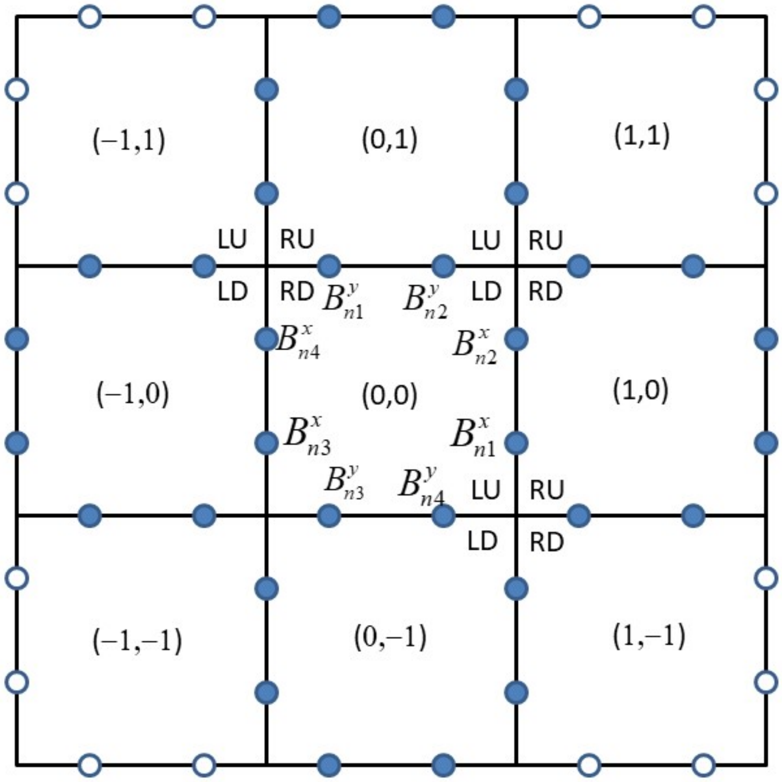
(−1,1)
(0,1)
(1,1)
LU
RU
LU
RU
LD
RD
B^y_{n1}
B^y_{n2}
LD
RD
B^x_{n4}
B^x_{n2}
(−1,0)
(0,0)
(1,0)
B^x_{n3}
B^x_{n1}
B^y_{n3}
B^y_{n4}
LU
RU
LD
RD
(−1,−1)
(0,−1)
(1,−1)

Fig. 2 shows the four states RU (right-up), LU (left-up), LD (left-down) and RD (right-down) that come together at a vertex. These four states contribute to the multidimensional Riemann problem at that vertex. (Such states are only shown for a few vertices in the figure.) The multidimensional Riemann problem gives us the z-component of the electric field at that vertex. The nodal points that contribute to the update of the central zone for the p=1 RKDG scheme are also shown by dots within each face. At each of those nodal points within the (0,0) zone we explicitly identify the magnetic field components that reside at those nodes. Only the filled dots at the nodal points truly contribute to the update of the nodal points that lie on the faces of the (0,0) zone.

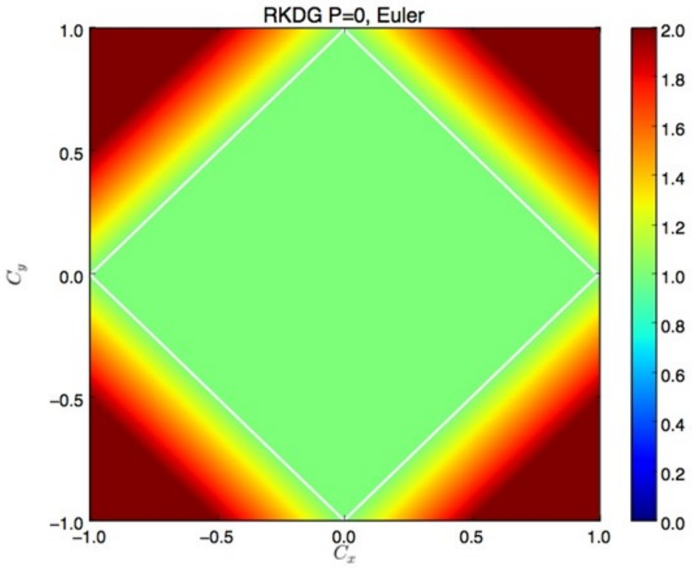

Fig 3 shows the domain of stability for the first order (P=0) DG scheme with forward Euler timestepping. The x- and y-axes of the plot show the CFL number in the x- and y-directions. The color shows the amplitude of the amplification factor. The white lines identify the boundary of the domain of stability. Within the domain of stability, the amplification factor is less than or equal to unity for all possible wave modes that can propagate on the mesh. The CFL number is just the radius of the largest circle (in the Euclidean norm) remaining within the stability region in Fig. 3.

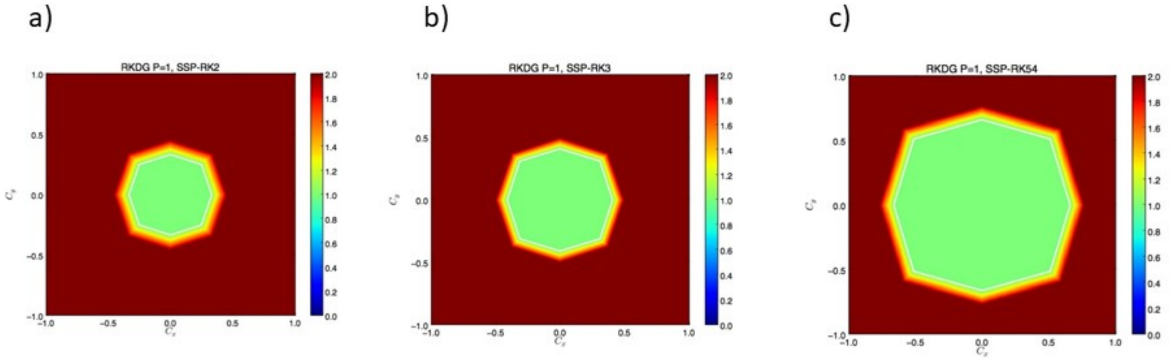

Fig. 4 shows the domain of stability for the second order (P=1) DG scheme with several different timestepping strategies. Figs. 4a and 4b show the result of using the second and third order SSP schemes from Shu and Osher. Fig. 4c shows the result of using the RK(5,4) scheme from Spiteri and Ruuth. The white curves identify the boundary of the domain of stability. The CFL number is just the radius of the largest circle (in the Euclidean norm) remaining within the stability region in Fig. 4.

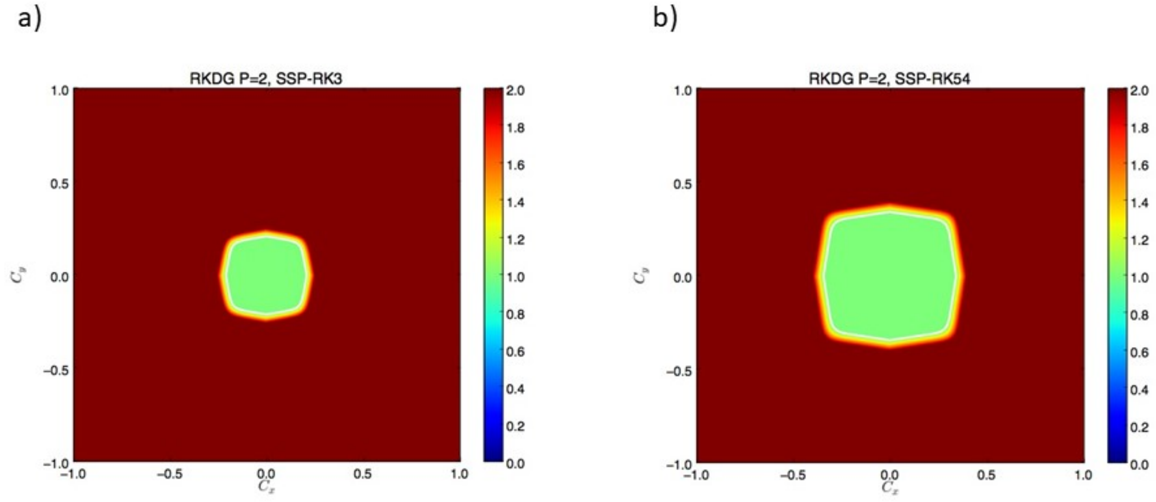

Fig. 5 shows the domain of stability for the third order (P=2) DG scheme with several different timestepping strategies. Fig. 5a shows the result of using the third order SSP scheme from Shu and Osher. Fig. 5b shows the result of using the RK(5,4) scheme. The white curves identify the boundary of the domain of stability. The CFL number is just the radius of the largest circle (in the Euclidean norm) remaining within the stability region in Fig. 5.

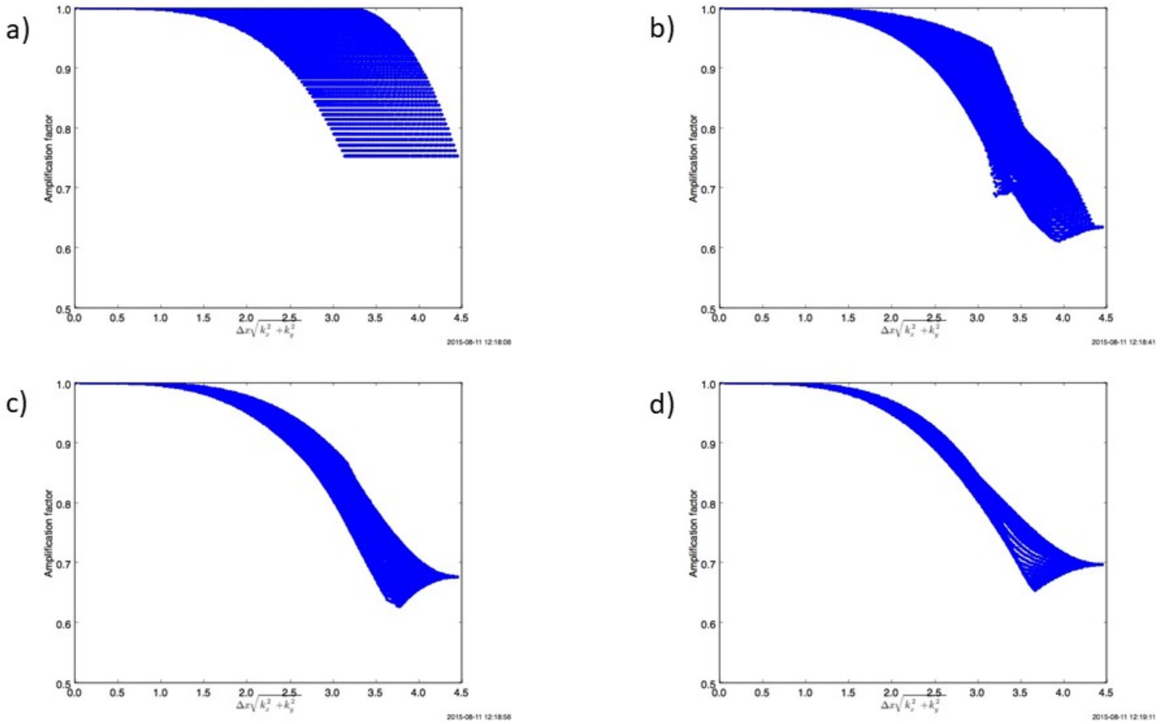

Figs. 6a, 6b, 6c and 6d show the result of such a wave propagation study when the velocity vector makes angles of 0°, 15°, 30° and 45° to the mesh for the second order (P=1) DG scheme with SSP-RK2. Figs. 6 and 7 use the same vertical scale so that the amplification factors at different orders can be cross-compared.

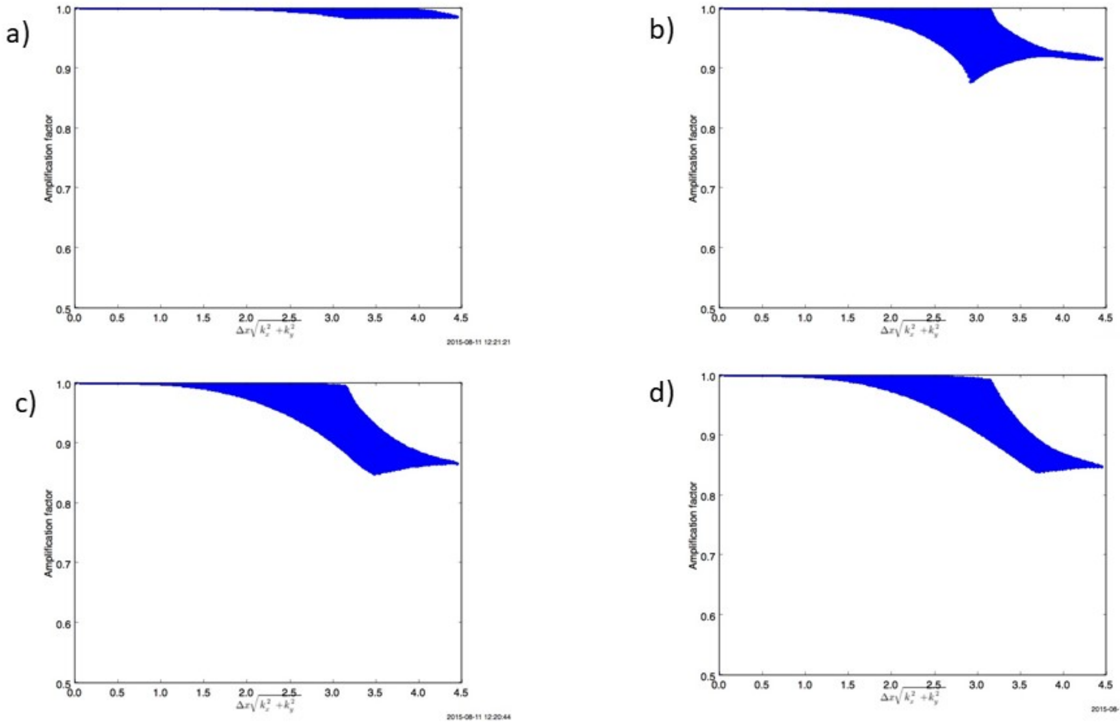

Figs. 7a, 7b, 7c and 7d are analogous to Fig. 6 but pertain to the third order (P=2) DG scheme with SSP-RK3. We see that the higher order scheme shows better wave propagation in all directions.

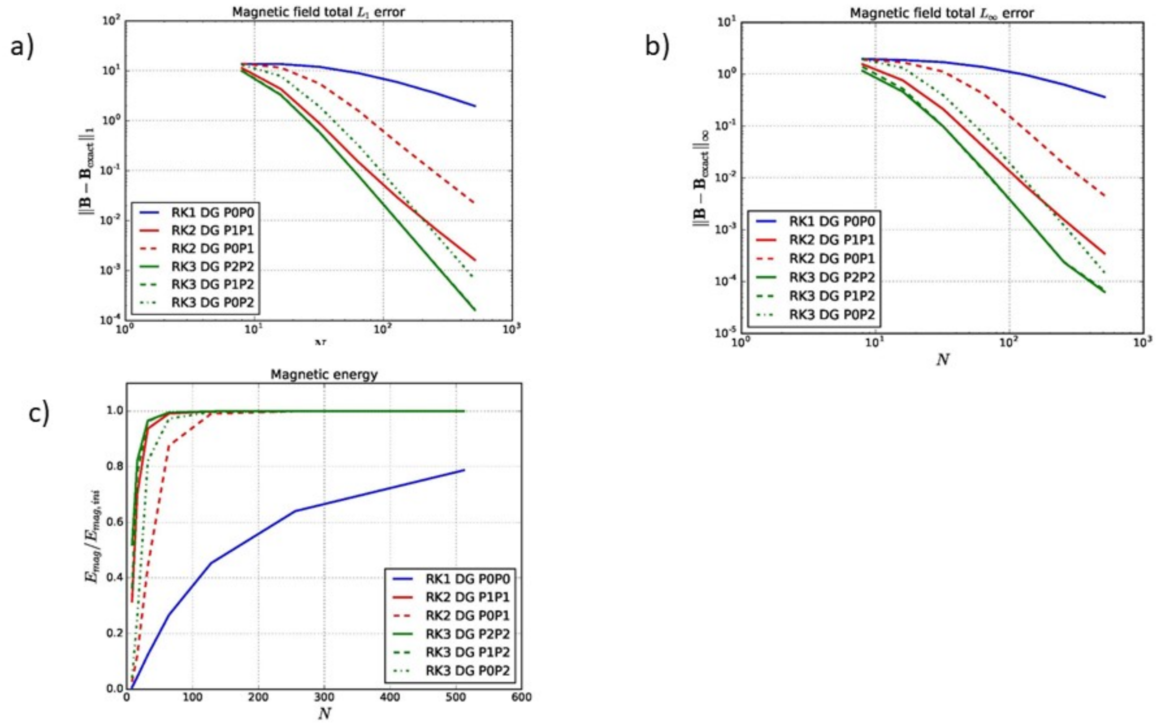

Fig. 8 shows all the data from Tables VI to IX in a single set of plots. Figs. 8a and 8b show the L_1 and L_∞ errors as a function of mesh size measured along one of the edges of the mesh. Fig. 8c shows the magnetic energy that is preserved on the mesh at the final time in the simulation as a function of mesh size.